

Delay Doppler SAR Focusing and Quantitative Quality Control of the Radar for Europa Assessment and Sounding: Ocean to Near-Surface (REASON) Sounding Data Product

Kirk M. Scanlan , Duncan A. Young, Gregor Steinbrügge , Scott D. Kempf, Cyril Grima, and Donald D. Blankenship

Abstract—Synthetic aperture radar (SAR) focusing will be a fundamental step in the analysis of the radar sounding datasets collected by the Radar for Europa Assessment and Sounding: Ocean to Near-surface (REASON) instrument as part of NASA’s upcoming Europa Clipper mission. Due to the flyby trajectory of the mission, REASON data acquisition will be distinct compared to other space-borne radar sounders, and therefore, require a tailored SAR focusing strategy. Here, we present a SAR focusing architecture based on the delay Doppler approach employed in US SHallow RADar (SHARAD) data analysis with the following modifications for REASON data idiosyncrasies; an interpolation to a constant ground track interval to account for REASON’s variable PRF; and an adaptive Doppler centroid estimation to account for the flyby geometry. The ability of our modified delay Doppler SAR focusing approach to focus space-borne datasets as well as its specific feasibility for REASON are demonstrated using both SHARAD and MARSIS datasets. In addition, we present a quantitative quality control framework based on pixel power probabilities and demonstrate how it can be leveraged to quantify the effects of SAR focusing and differentiate focused results generated with different processing parameters. Finally, we revisit and discuss the assumption of depth-independent SAR focusing implicit in the choice to construct a REASON SAR focusing approach based on the delay Doppler method and provide a comparison with depth-dependent SAR focusing for a simplified acquisition geometry.

Index Terms—Europa Clipper, radar remote sensing, radar signal processing, spaceborne radar, synthetic aperture radar.

I. INTRODUCTION

THE past decades have seen active radar sounding measurements become a valuable tool in the study of planetary

surfaces and subsurfaces [1]–[5]. Key to this has been the existence of specialized data processing techniques [i.e., synthetic aperture radar (SAR) focusing] used to increase the resolution of the resulting radar images without requiring large physical radar antennae. A wide variety of SAR focusing strategies exist for use with both space-borne and airborne datasets [2]–[4], [6]–[9]. All of these strategies involve the creation of synthetic apertures within which Doppler information is leveraged to recombine energy reflected from surface and subsurface targets as the radar moves along its track. This recombination narrows the effective beam pattern, collapses diffraction hyperbolae and improves the alongtrack resolution of the output image. The purpose of this article is twofold; first to investigate a SAR focusing methodology suitable for the analysis of future REASON datasets collected as part of NASA’s upcoming Europa Clipper mission and second, to develop a quality control framework that can be used to quantitatively assess the effects of changing the parameters used in the generation of those focused radar sounding datasets.

The Radar for Europa Assessment and Sounding: Ocean to Near-surface (REASON) instrument [10], [11] to be carried onboard NASA’s Europa Clipper spacecraft as well as the Radar for Icy Moons Exploration (RIME) instrument [12] to be carried onboard ESA’s JUpiter ICy moons Explorer (JUICE) spacecraft represent the next generation of space-borne planetary radar sounders following those currently in orbit around the Moon [13] and Mars [14]–[17]. In addition to its ability to collect sounding data at both HF (9 MHz center frequency, 1 MHz bandwidth) and VHF (60 MHz center frequency, 10 MHz bandwidth) data simultaneously, REASON operates at altitudes between 1000 and 25 km above Europa’s surface. This large range of operating altitudes is a consequence of the flyby (as opposed to orbital) design of the Europa Clipper campaign and serves to minimize the amount of time the spacecraft is exposed to high levels of radiation in the immediate vicinity of Europa [18]. The flyby geometry imposes distinct operational constraints on the REASON instrument that produce idiosyncrasies in the resulting datasets that must be accounted for during SAR data processing. As the RIME instrument will also operate under similar geometries during JUICE flybys of Europa, the SAR data processing techniques discussed for REASON are equally applicable to these datasets as well.

Manuscript received March 12, 2021; accepted April 2, 2021. Date of publication April 9, 2021; date of current version May 6, 2021. This work was supported in part by the REASON investigation of the Europa Clipper project under NASA contract NNM16AA26C with the University of Texas at Austin as well as the Radar for Icy Moon Exploration investigation of the JUICE project under NASA Jet Propulsion Laboratory (JPL) research support agreement RSA No. 1656676 as part of NASA prime contract NNN12AA01C. (Corresponding author: Kirk M. Scanlan.)

Kirk M. Scanlan, Duncan A. Young, Scott D. Kempf, Cyril Grima, and Donald D. Blankenship are with the University of Texas Institute for Geophysics, University of Texas at Austin, Austin, TX 78758 USA (e-mail: kirk.scanlan@utexas.edu; ducan@ig.utexas.edu; scottk@ig.utexas.edu; cyril.grima@utexas.edu; blank@ig.utexas.edu).

Gregor Steinbrügge is with the Department of Geophysics, Stanford University, Stanford, CA 94305 USA (e-mail: gbs@stanford.edu).

Digital Object Identifier 10.1109/JSTARS.2021.3072276

This work is licensed under a Creative Commons Attribution 4.0 License. For more information, see <https://creativecommons.org/licenses/by/4.0/>

The Lunar Radar Sounder (LRS) instrument onboard the SELENE spacecraft (5 MHz center frequency, 2 MHz bandwidth) [13], the Mars Advanced Radar for Subsurface and Ionospheric sounding (MARSIS) instrument onboard Mars express (1.8, 3, 4, and 5 MHz center frequencies, 1 MHz bandwidth) [14], [15], and the SHallow RADar (SHARAD) instrument onboard the Mars Reconnaissance Orbiter (20 MHz center frequency, 10 MHz bandwidth) [16], [17] all employ a constant pulse repetition frequency (PRF) (20 Hz for LRS, 127 Hz for MARSIS, and 700Hz for SHARAD) consistent with achieving their respective science objectives. The REASON PRF, however, will vary as a function of altitude in an attempt to maintain the Doppler frequency bandwidth required for removing alongtrack surface targets at ranges equivalent to a nadir subsurface reflector at 3 km depth in ice during on-ground SAR processing [19]. Furthermore, because Europa Clipper is always either approaching or receding from Europa over the course of a flyby, unlike for LRS and SHARAD, the Doppler frequencies of targets in the middle of an arbitrary synthetic aperture will not be zero (the sole exception being for a synthetic aperture centered on the position of closest approach). The combination of these two factors is distinct to REASON and must be reflected in the design of a suitable SAR focusing algorithm.

The remainder of this article is structured as follows; Section II outlines the basics of SAR focusing, the basic delay Doppler SAR approach [6] and the steps taken to modify it for REASON data idiosyncrasies. In Section III, we apply our modified delay Doppler SAR (mDD-SAR) approach to data from two SHARAD orbits. We then first, qualitatively compare our results against each other as well as to standard published SHARAD results and second, introduce a quantitative quality control framework designed to aid in evaluating the effects of changing different processing parameters within the SAR focuser (namely the aperture length). After demonstrating that the mDD-SAR method can be used to focus standard SHARAD data, in Section IV we perform an in-depth investigation of the suitability of the modifications to ensure they are capable of addressing REASON data idiosyncrasies. Finally, in Section V, we discuss the possible limitations in the proposed mDD-SAR approach with respect to depth-dependent SAR focusing, and in Section VI we summarize the conclusions of this work.

II. SAR FOCUSING AND THE MODIFIED DELAY DOPPLER APPROACH

Delay Doppler SAR focusing is the standard method used in the US processing of SHARAD data [6]. However, other approaches used in the reduction of space-borne radar sounding measurements include depth-dependent matched filter focusing, used in the reduction of LRS data [9], as well as chirp scaling, used in the Italian analysis of SHARAD data [17]. The basic delay Doppler technique was chosen as the starting point for prospective REASON SAR focusing both because of its simplicity, and therefore adaptability, as well as its heritage with SHARAD. There are also substantial volumes of minimally-processed SHARAD data available through NASA's Planetary Data System (PDS) with which to develop and test the approach.

A simplified representation of typical orbital (as opposed to flyby) space-borne radar sounding data acquisition at five points (moving from A through E) within a synthetic aperture is presented in Fig. 1(a). At each position, the radar transmits a signal that illuminates the surface and subsurface of the target body and generates a reflection. The alongtrack resolution of the radargram is related to the size of the illuminated area, where a smaller illuminated area implies finer spatial resolution. For a flat specular surface, the illuminated portion of the target generating the reflected echo is defined by the Fresnel zone whose radius (R_f) is given by

$$R_f = \sqrt{\left(h + \frac{\lambda}{4}\right)^2 - h^2} \approx \sqrt{\frac{\lambda h}{2}} \text{ for } h \gg \lambda \quad (1)$$

where h represents the altitude of the platform and λ is the free-space radar wavelength [20]. In practice, due to a combination of factors (including interface roughness, wide antenna beam patterns, and long chirp signals), the radar-illuminated area for a single range resolution cell on the surface is typically much larger than the Fresnel zone and characterized by the pulse-limited footprint [4], [20] whose radius (R_{PL}) is given by

$$R_{PL} = \sqrt{\left(h + \frac{c}{BW}\right)^2 - h^2} > R_f \quad (2)$$

where c is the speed of light and BW is the radar signal bandwidth [11]. Because the pulse-limited footprint is large, an individual point on the surface (O in Fig. 1) will fall within the pulse-limited footprint of multiple radar measurements made at different orbital positions (as signified by the dash-dot lines) and diminish the alongtrack resolution of the radargram. The goal of SAR focusing is to combine range-compressed echoes from a common mid-aperture target (position O), measured across multiple overlapping footprints within the synthetic aperture (A through E). This narrows the alongtrack radar beam pattern (the size of the beam pattern in the cross-track direction is not affected) and decreases the size of illuminated area from its pulse-limited width to something that, for a rough interface, can be less than the Fresnel zone.

Coherent superposition of the echoes from a target in the middle of the synthetic aperture relies on being able to predict the corresponding Doppler frequency phase shift for that target at every measurement position within the aperture. The Doppler frequency describes the rate at which the recorded phase of the target echo varies as a function of the time during which the target is illuminated by the radar or is within the extent of the synthetic aperture. For an ideal circular orbit [see Fig. 1(a)], the change in the phase associated with mid-aperture target echoes is largest towards the edge of the synthetic aperture (represented by positions A and E), implying larger Doppler frequency magnitudes at these positions. As the spacecraft approaches the mid-aperture position (positions B and D), there is less variation in the target echo phase and the magnitude of the Doppler frequency decreases. At closest approach (position C), the Doppler frequency is zero. As phase is related to the distance between the instrument and the mid-aperture target, Doppler frequencies (f_D) can be calculated from the change in

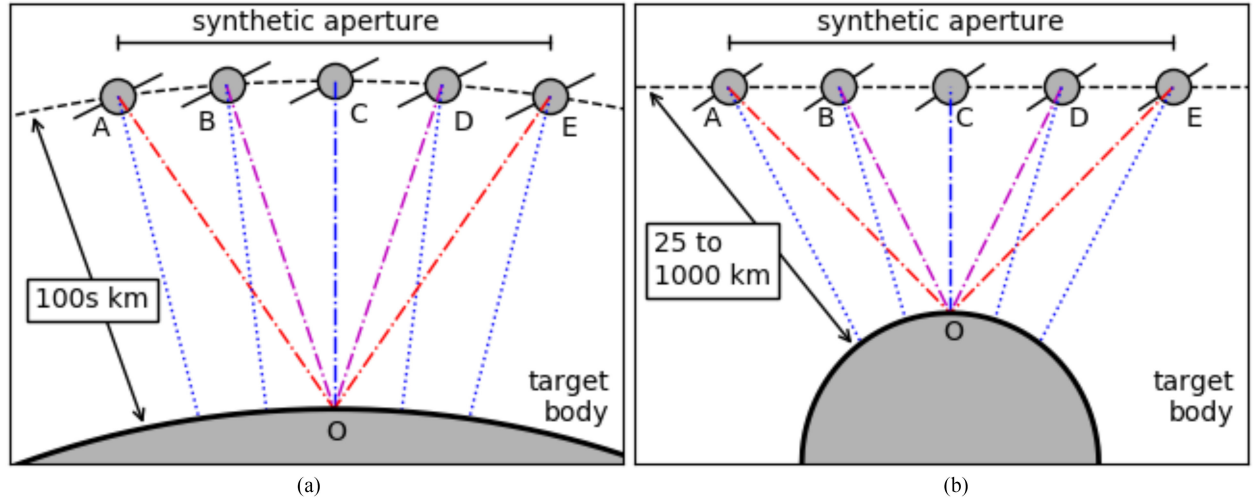


Fig. 1. Simplified geometry associated with space-borne radar sounding of point O on the surface of the target body with (a) an orbital instrument (e.g., SHARAD) and (b) a flyby instrument (e.g., REASON and RIME). Dotted lines represent the nadir propagation path while dash-dot lines represent select raypaths within an illustrative pulse-limited footprint. Colors for the dot-dashed lines represent the relative magnitude of the Doppler frequencies for echoes from point O (warmer colors represent greater Doppler frequency magnitudes), but will not be equivalent between the orbital and flyby geometries. As the spacecraft moves from left to right (A through E), note that in contrast to the orbital geometry [a], the only position where the Doppler frequency at the mid-aperture position can be expected to zero for a flyby trajectory is at the position of closest approach [i.e., the situation shown in b)].

this distance across the synthetic aperture [2], [7], [8] using

$$f_D = -\frac{2}{\lambda} \frac{dR_t(t)}{dt} \quad (3)$$

where $R_t(t)$ is the one-way range from the spacecraft to the target as a function of time within the aperture. By convention, Doppler frequencies are defined as being positive as the platform approaches the target [i.e., the distance to the target decreases; positions A and B in Fig. 1(a)] and negative as the target recedes (i.e., the distance to the target increases; positions D and E) [1], [2], [8]. The Doppler phase shift (Φ) is defined by

$$\Phi = e^{-j \frac{4\pi [R_t(t) - R_0]}{\lambda}} \quad (4)$$

where R_0 is the distance from the spacecraft to the target at the mid-aperture position [2], [7], [8].

In conventional SHARAD delay Doppler SAR focusing, Doppler phase shifts are calculated using the change in the distance to the mid-aperture surface position only and ignore the effects of radar wave refraction in the subsurface [6]. This stands in contrast to matched filter SAR focusing, which attempts to account for refraction at the surface interface for subsurface targets [2], [7]–[9]. SHARAD delay Doppler SAR focusing also assumes that fast-time frequencies and Doppler frequencies are independent, even while this is strictly not true [3]. Under these assumptions, SAR focusing can be achieved in two serial migrations; a fast-time (delay) migration applied as a multiplication between the calculated Doppler phase shifts and the radar data when expressed in the fast-time frequency/slow-time domain; and an azimuth (Doppler) migration applied as a multiplication between the Doppler phase shifts and the delay migrated radar data expressed in the fast-time/Doppler frequency domain. In conventional SHARAD data processing, after azimuth migration a Hann window is used to suppress sidelobes around zero Doppler frequency and a focused range line is generated after

multilooking the Hann filtered result to a preset Doppler bandwidth [6].

In anticipation of the idiosyncrasies in future REASON datasets, the basic SHARAD delay Doppler approach is modified with two additional steps; one occurring prior to migration and one after both delay and azimuth migration (see Fig. 2). The first modification is a linear interpolation of both telemetry and radar data to a constant ground track trace spacing and is designed to account for REASON's variable PRF. The second modification is an estimation of the mid-aperture surface target's Doppler frequency (i.e., the Doppler centroid) based on the tangent to the $R_t(t)$ curve. To this end, consider a synthetic aperture comprised of positions A, B, and C in Fig. 1. For the orbital geometry [see Fig. 1(a)], the point of closest approach will correspond to position B and the mid-aperture Doppler frequency will be zero. In contrast, for a flyby geometry [see Fig. 1(b)] the point of closest approach will be position C and the mid-aperture Doppler frequency will be nonzero. Correctly estimating the Doppler centroid is essential such that the azimuth-migrated result can be extracted for the correct Doppler frequency. The $R_t(t)$ profile across the synthetic aperture in the mDD-SAR algorithm is calculated from the interpolated telemetry data using spherical coordinates.

The modifications made to the conventional SHARAD delay Doppler approach also affect the types of user-defined processing parameters required as inputs. In lieu of a SAR column posting interval defining the distance between range lines in the output radargram [6], the mDD-SAR approach requires a ground track interpolation interval (defined in meters) and a SAR focusing interval (the interval between interpolated range lines centering subsequent apertures). The product of these two inputs defines the ground track distance between range lines in the SAR focused output. For example, if the ground track interpolation interval is set to ten meters and the SAR

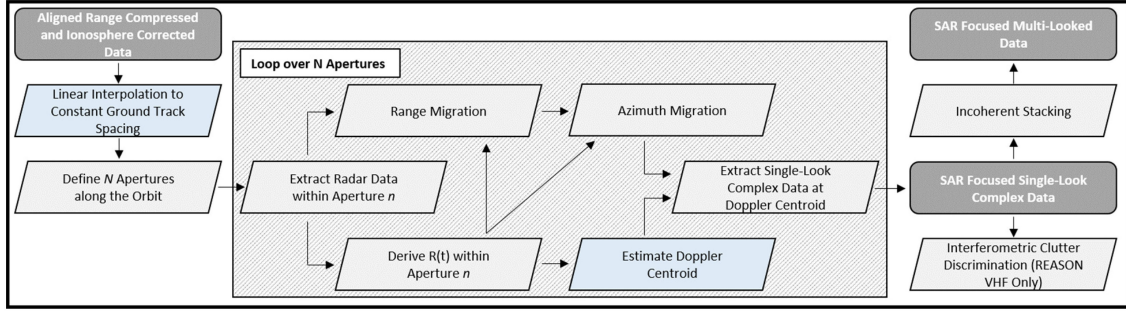


Fig. 2. Block diagram illustrating the mDD-SAR focusing algorithm for REASON data as well as the envisioned output data products. Additional steps required for REASON data idiosyncrasies are highlighted in blue.

focusing interval is set to five, the output SAR focused radargram will exhibit a 50 m ground track spacing between range lines. Furthermore, multilooking is not explicit in the mDD-SAR algorithm so a Doppler bandwidth is no longer a required input [6]. Multilooking is omitted from the mDD-SAR approach in order to produce the single-look complex-valued datasets that are required for clutter discrimination using interferometry [19], [21]. However, multilooked radargrams are produced through incoherent stacking of the single-look outputs (see Fig. 2).

III. FOCUSING SHARAD DATASETS

Prior to performing a detailed investigation into the suitability of the delay Doppler modifications for REASON, here we first demonstrate that the algorithm described in Section II can be used to focus space-borne SAR datasets. This is accomplished using two illustrative SHARAD orbits; 10589 (the entire orbit; Fig. 3) and 10798 (between 42.00°N and 48.03°N; Fig. 4). SHARAD orbit 10589 covers a portion of the Martian Northern Polar layered deposits (NPLD) near Gemina Lingula and was selected because of the extreme topographical variability along the ground track (a flat-lying surface adjacent to cliffs) as well as the prevalence of subsurface reflectors within the NPLD. The portion of SHARAD orbit 10798 used in this study covers the northern edge of Tempe Fossae and was selected because it presents with a surface roughness similar to that of Europa ridged terrain [22], [23]. Unprocessed data for these two orbits were downloaded from the PDS and range compression and ionospheric correction was performed following standard US SHARAD data processing methods [24], [25]. The range compressed and ionosphere-corrected radargrams [Figs. 3(a) and 4(a)] are the inputs for mDD-SAR focusing. SAR focusing is performed using three different aperture lengths: 5 km [see Figs. 3(b) and 4(b)], 15 km [see Figs. 3(c) and 4(c)], and 30 km [see Figs. 3(d) and 4(d)]. The ground track interpolation interval is kept constant at 10 m and each interpolated range line is focused (i.e., the SAR focusing interval is one). To suppress speckle, the radargrams in Figs. 3 and 4 have been incoherently stacked (multilooked) to an along-track range line spacing of 400 m.

A. Qualitative Comparison

As expected, compared to the range compressed and ionosphere corrected radargrams [see Figs. 3(a) and 4(a)], SAR

focusing of both SHARAD orbits yields a dramatic improvement in echo power while collapsing diffraction hyperbola. However, there are noticeable differences between the focused radargrams as the aperture length is progressively varied.

The most prominent difference is the change in echo amplitudes, which is most clearly visible in the orbit 10589 results (see Fig. 3). For short apertures [i.e., 5 km; Fig. 3(b)] similar to the Fresnel zone diameter (~ 6 km for SHARAD at 300 km altitude), SAR focusing highlights reflections from flat-lying, specular targets (in this case associated with the NPLD surface and internal layers between 0 and 20 s, 50 and 60 s, and > 65 s). In areas of more variable topography (e.g., between 20 and 50 s) only the peaks or the base of troughs in the surface topography are enhanced by SAR focusing as they generate diffraction hyperbola most similar to point targets. Extended, steeply dipping surface and subsurface interfaces are not well imaged when using the shortest SAR aperture. As the aperture length is increased [to 15 km in Fig. 3(c) and to 30 km in Fig. 3(d)], the specular target echo strengths progressively weaken, leading to loss of deep subsurface reflections from within the NPLD. In contrast, reflection strengths from point target-like features on the surface do not significantly vary. This is a direct consequence of the along-track angular distribution of reflections from these two types of targets as discussed and demonstrated in [7] and [9]. While reflection strengths for flat-lying targets are reduced when the aperture length is increased, the imaging of dipping surface features is improved (e.g., the small surface prominence at 25 s and the incised valley at 60 s), which enhances along-track resolution. A similar decrease in specular echo strength with increasing aperture length can be observed in the orbit 10798 results [e.g., near 13 and 80 s in Fig. 4(b)–4(d)], but is overall less noticeable due to the absence of numerous extended specular targets. The ability to better resolve dipping features through SAR focusing with longer apertures is also observed in the 10798 radargram (e.g., the feature at 30 s and 1100 fast-time samples).

In addition to signal, noise levels within the radargrams are affected by mDD-SAR focusing with different aperture lengths and the effects are similar between the two SHARAD orbits. Recall that the same amount of incoherent stacking has been applied to each focused radargram in Figs. 3 and 4 in order to reduce speckle. Noise levels in the 5 km aperture results exhibit the lowest absolute power of any focused radargram, but also the greatest variability. As the aperture is lengthened, noise levels

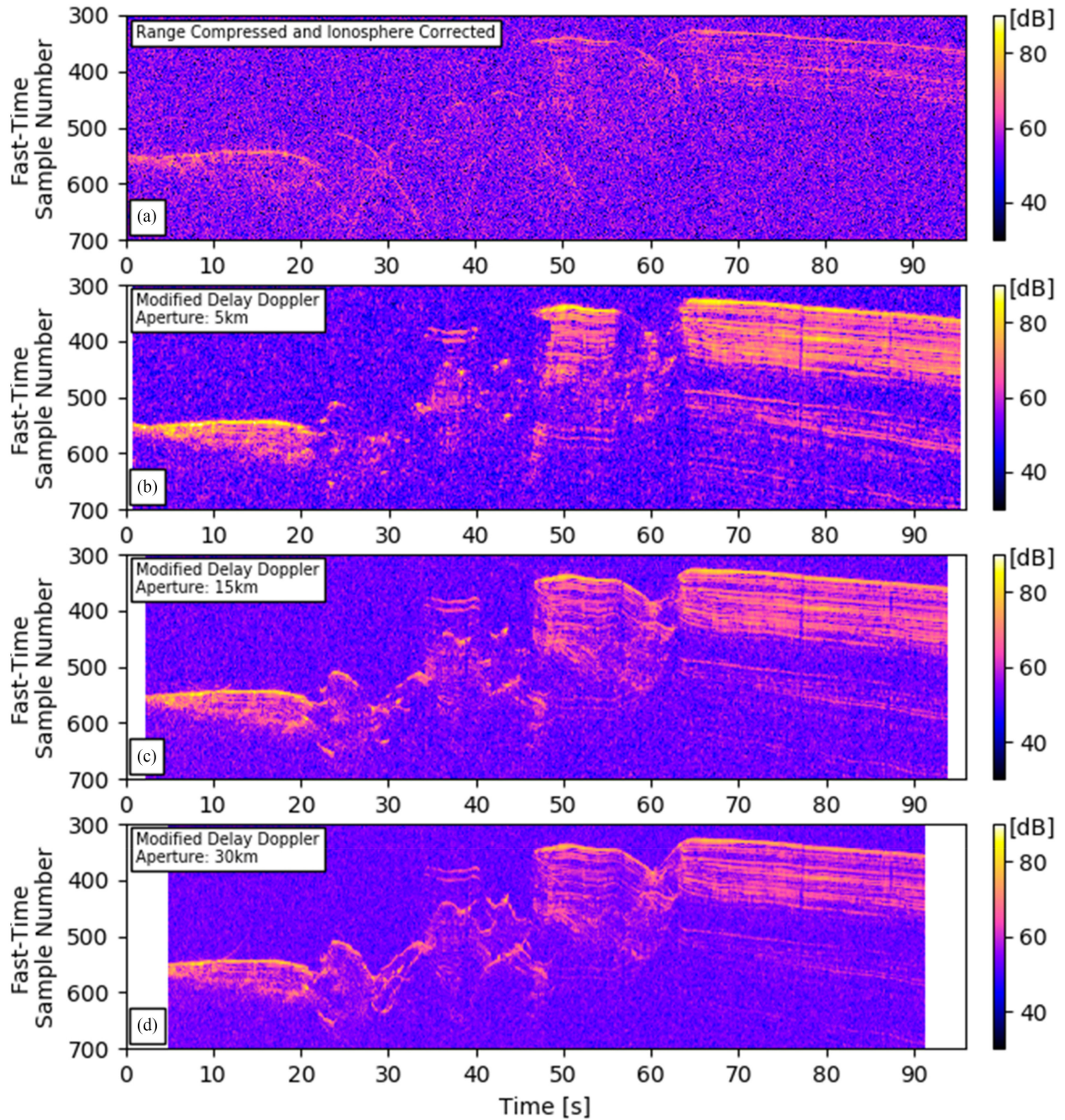


Fig. 3. SHARAD orbit 10589 after (a) range compression and ionosphere correction, and mDD-SAR focusing with (b) 5 km-long aperture, (c) 15 km-long aperture, and (d) 30 km-long aperture. Note a decrease in SAR gain is accompanied by an ability to better resolve steeply-dipping surface slopes as the aperture length is increased.

homogenize around a consistent value yielding a smoother noise background.

Radargrams for SHARAD orbits 10589 and 10798 after standard US [6] and Italian [16], [26], [27] SAR processing are also available for download from the PDS and are presented in Figs. 5 (US) and 6 (Italian). PDS radargram amplitudes have not been modified from what is contained in the PDS data files. Also note that Italian RDR data products have a different fast-time sampling rate than either US RDR data products or those produced as part of this study. The US RDR radargrams (see Fig. 5) are produced using an 8.774 s long aperture (~ 30 km

for a MRO velocity of 3.4 km/s), an output range line spacing of 460 m, and 7 looks, while the Italian RDR radargrams (see Fig. 6) are processed such that the nominal alongtrack resolution is 300 m.

The most noticeable difference between the mDD-SAR focused radargrams (see Figs. 3 and 4) and those from the PDS (see Figs. 5 and 6) is the inclination of the radargrams. This inclination likely results from the standard SHARAD processing defining MRO altitudes relative to the Mars orbiter laser altimeter digital terrain model (DTM) [6] while this analysis, using only SHARAD telemetry data, defines platform altitudes

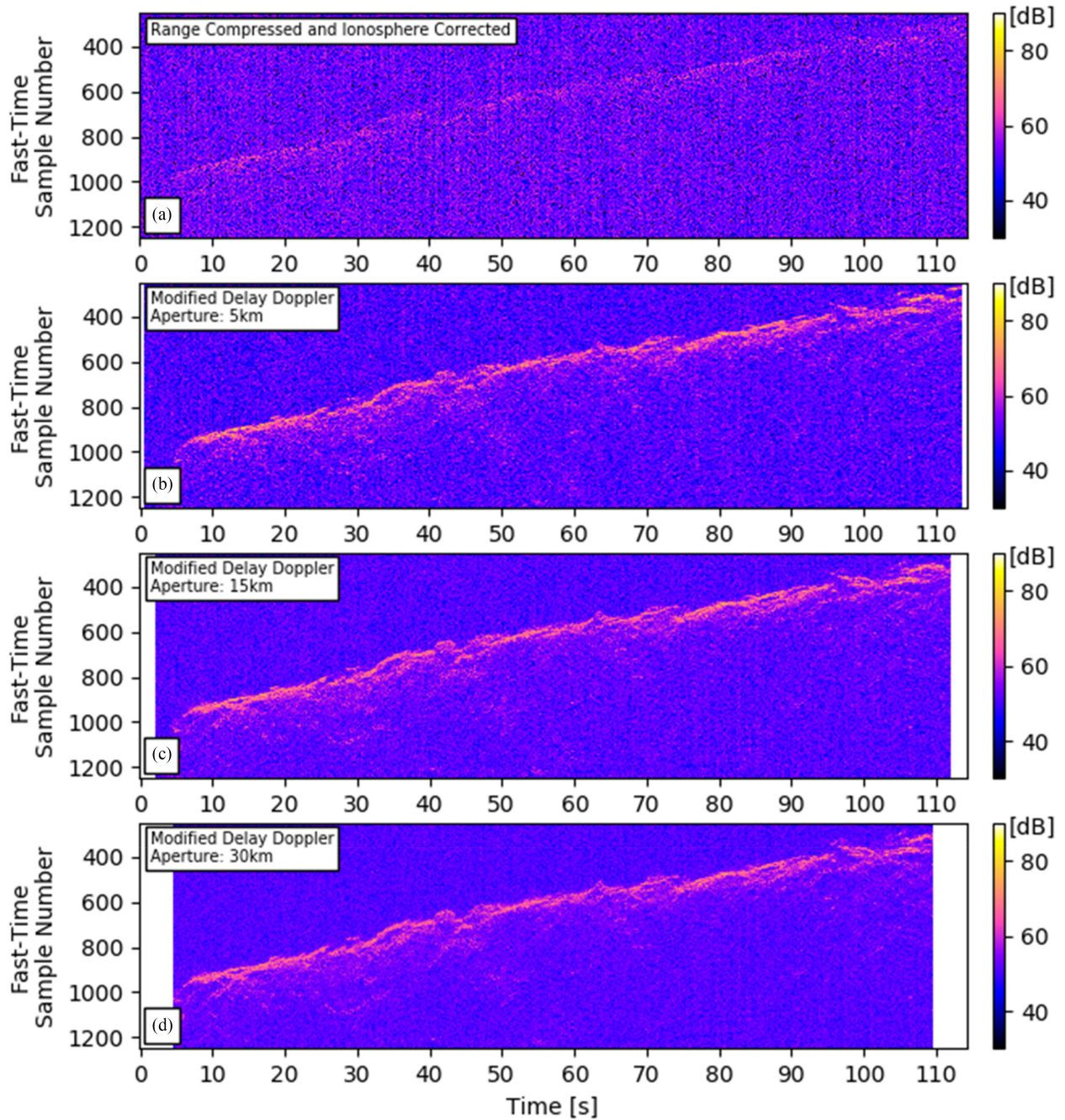


Fig. 4. SHARAD orbit 10798 after (a) range compression and ionosphere correction, and mDD-SAR focusing with (b) 5 km-long aperture, (c) 15 km-long aperture, and (d) 30 km-long aperture. Note that, compared to Fig. 3, SAR gain is much more consistent as a function of aperture length.

relative to the IAU2000 Martian ellipsoid. The decision was made to rely solely on SHARAD telemetry data instead of a pre-existing DTM for this analysis because this situation more in keeping with what is expected to be immediately available for future REASON data.

Beyond the small tilt, versions of the mDD-SAR radargrams qualitatively agree very well with the US SHARAD RDR radargrams (see Fig. 5). The SHARAD orbit 10589 US RDR radargram [see Fig. 5(a)] most resembles a slightly less noisy version of our 15 km aperture mDD-SAR result [see Fig. 3(c)]. The extent of the visible subsurface reflectors in the NPLD (i.e.,

70 to 80 s) as well as the degree to which dipping surface features are not being imaged (i.e., the small prominence at 25 s and the valley at 60 s) is similar between the two radargrams. It is worthwhile to note that the 30 km aperture mDD-SAR radargram [see Fig. 3(d)] yields more a well-defined surface in the vicinity of steeply dipping terrain than the standard US RDR data product but less subsurface information. The SHARAD orbit 10798 US RDR radargram [see Fig. 5(b)] appears very similar to both the 15 and 30 km aperture mDD-SAR radargrams [see Figs. 4(c) and 4(d)]. The only noticeable differences are related to reflections recorded after the surface (at higher fast-time sample

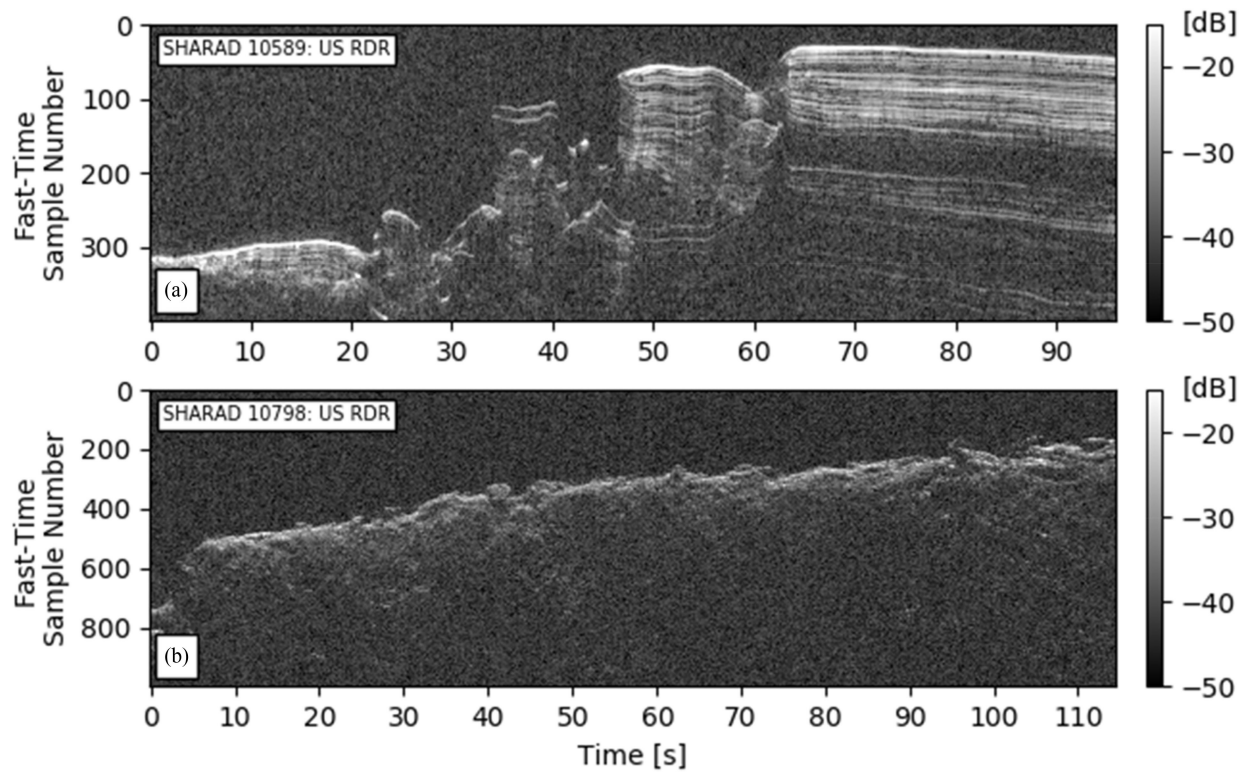


Fig. 5. Standard US SAR focused radargrams for SHARAD orbits. (a) 10589. (b) 10798.

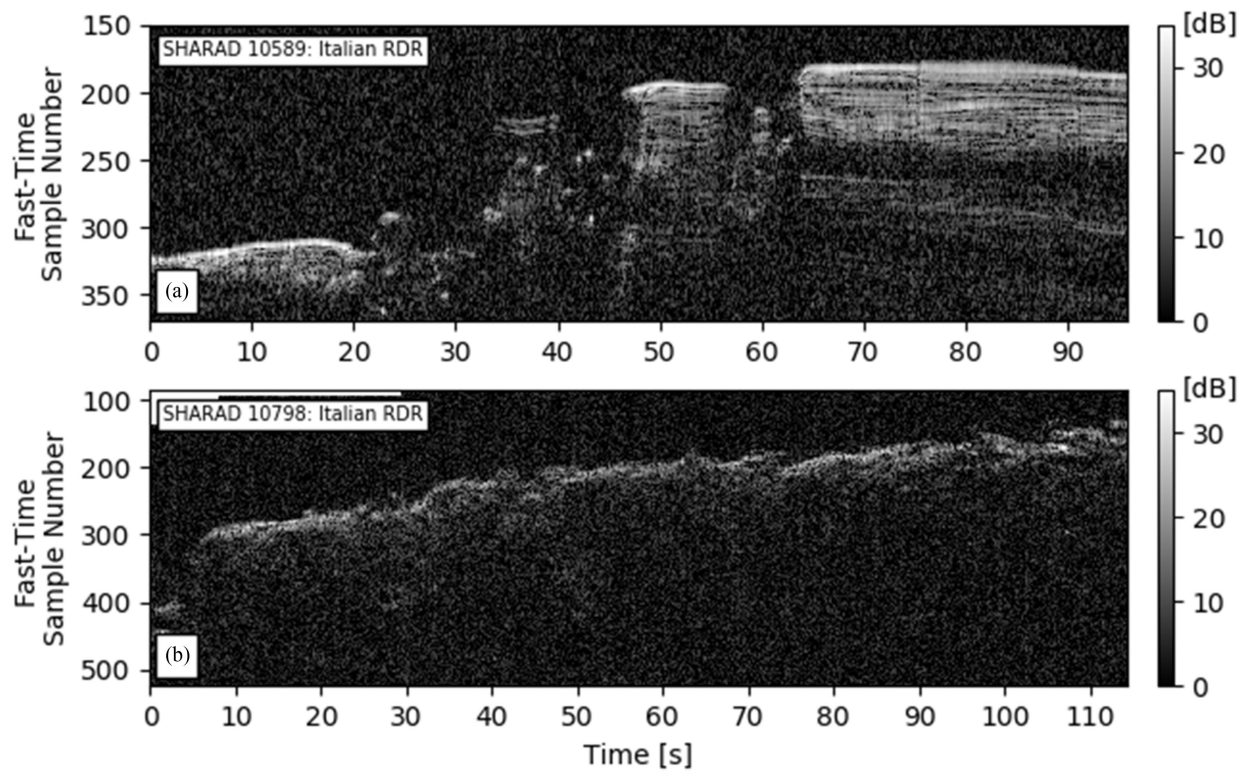


Fig. 6. Standard Italian SAR focused radargrams for SHARAD orbits. (a) 10589. (b) 10798.

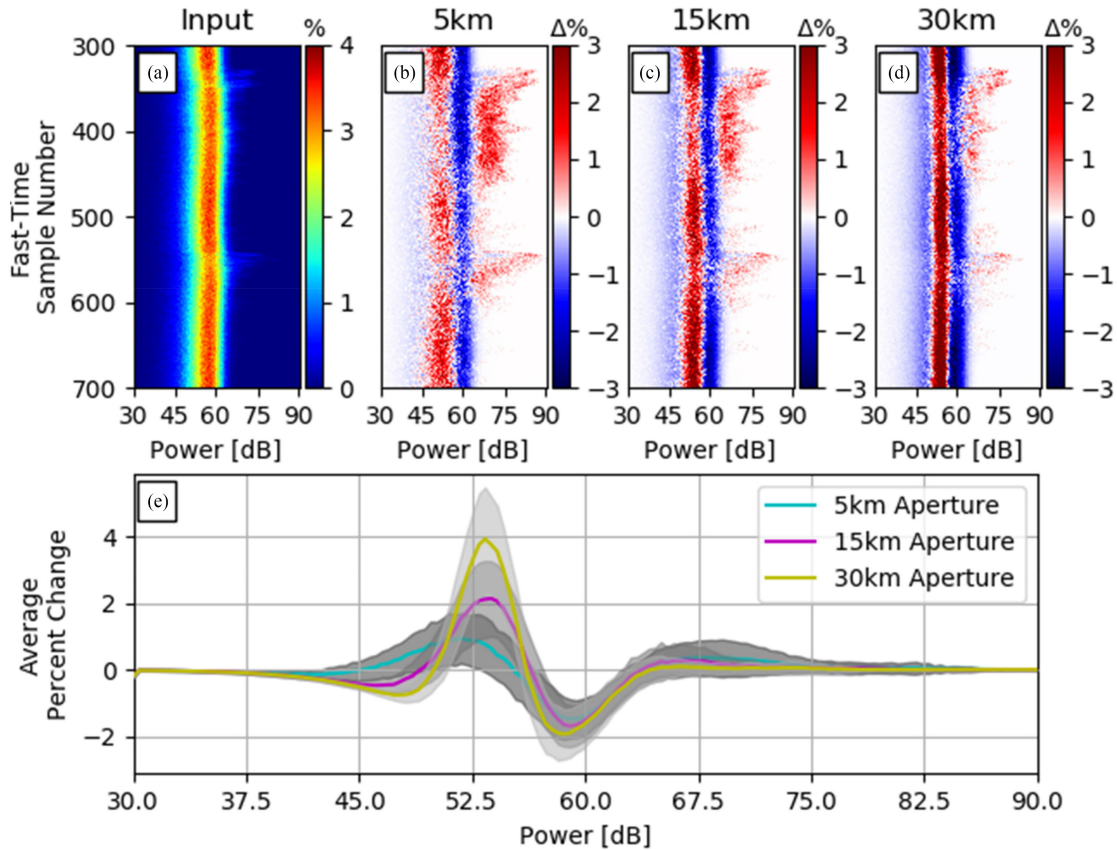


Fig. 7. Pixel power probability quality control results for SHARAD orbit 10589. (a) Probability of fast-time pixel powers in the range compressed and ionosphere-corrected radargram, the change in fast-time pixel power probabilities after mDD-SAR focusing with a (b) 5 km, (c) 15 km, (d) 30 km aperture, and (e) the change in pixel power probability for an arbitrary pixel. The vertical red bands in (b), (c), and (d) effectively represent the noise floor.

numbers), which are slightly more well defined in the 30 km aperture modified delay Doppler result [i.e., the small dipping feature between 40 and 45 s and 800 to 900 fast time samples in Fig. 4(d)].

Turning to the Italian RDR data products, both the orbit 10589 [see Fig. 6(a)] and 10798 [see Fig. 6(b)] radargrams most closely resemble the mDD-SAR results produced using a 5 km aperture [see Figs. 3(b) and 4(b), respectively]. The Italian RDR data product has difficulty imaging the surface in areas of rough topography [i.e., between 20 and 45 s in Fig. 6(a)] similar to what is observed in mDD-SAR focusing with the shortest aperture [see Fig. 3(b)]. Even though the Italian RDR surface definition along orbit 10589 is similar to that of 5 km aperture mDD-SAR result, the modified delay Doppler performs much better at recovering deeper subsurface reflections from within the NPLD. In terms of SHARAD orbit 10798, the 5 km-long aperture mDD-SAR radargram slightly outperforms the Italian RDR data product in terms of surface definition [compare Figs. 4(b) and 6(b) between 35 and 60 s], but overall, the results are fairly similar.

B. Quantitative Quality Control

In space-borne planetary radar sounding data, how to quantify the effects of SAR focusing with different parameters is not straightforward. SAR focusing is designed to re-organize energy in 2-D (both in slow-time and in fast-time) and the unfocused

and focused radargrams will have a different number of range lines. Therefore, whatever metric is used for quantitative quality control of the focused results must be capable of highlighting the restructuring of energy but be insensitive to changes in the slow-time discretization of the radargram. Here, we use the pixel power probability metric originally introduced in [28].

The pixel power probability quality control metric is used to quantify how power levels vary for individual fast-time pixels as well as an average pixel as a function of data processing. To isolate the effects of SAR focusing, similar to [28] we normalize pixel power probabilities to those observed in the input range compressed and ionosphere corrected radargram. The results for SHARAD orbits 10589 and 10798 are presented in Figs. 7 and 8, respectively. Figs. 7(a) and 8(a) present the likelihood that a specific fast-time pixel exhibits a specific power in the input, unfocused radargram, while Fig. 7(b)–(d) and Fig. 8(b)–(d) present the changes in individual fast-time pixel power likelihood after mDD-SAR focusing with the different aperture lengths. Finally, Figs. 7(e) and 8(e) present the mean change in power likelihood and standard deviation for an arbitrary pixel [fast-time average of Fig. 7(b)–(d) and Fig. 8(b)–(d)].

The main features of mDD-SAR focusing that are highlighted by the pixel power probability metric are similar for both SHARAD orbits [see Figs. 7 and 8]. First there is the increased likelihood of low power pixels (near 53 dB for orbit 10589 and 52 dB for orbit 10798) that corresponds to a decrease in the noise

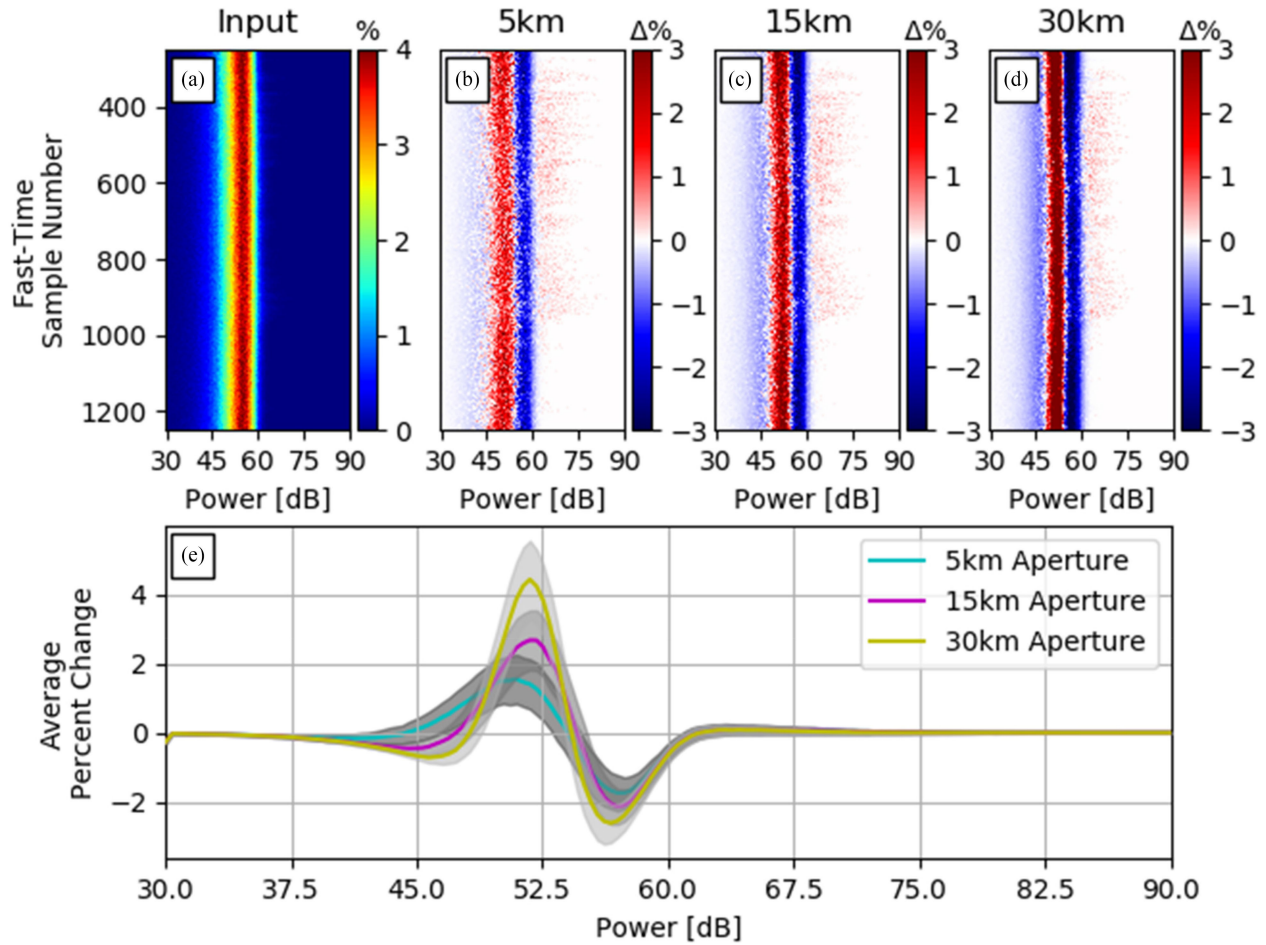


Fig. 8. Pixel power probability quality control results for SHARAD orbit 10798. (a) Probability of fast-time pixel powers in the range compressed and ionosphere-corrected radargram, the change in fast-time pixel power probabilities after mDD-SAR focusing with a (b) 5 km, (c) 15 km, and (d) 30 km aperture, and (e) the change in pixel power probability for an arbitrary pixel. The vertical red bands in (b), (c), and (d) effectively represent the noise floor.

floor. Second, there is the decreased likelihood of intermediate power pixels (across a band centered on 59 dB for orbit 10589 and 57 dB for orbit 10798) that implies SAR focusing is moving energy out of this power range (either towards the noise floor or to enhance signal). Finally, there is an increased likelihood of high power pixels associated with surface and subsurface echoes, which represents the SAR gain. The cumulative impact of these features are then focused radargrams with a greater separation between the noise floor and the strengths of the reflections of interest, leading to a higher signal-to-noise ratio (SNR). The patterns associated with the decrease in the noise floor as well as the reduction in pixels of intermediate power are similar for both orbits, while where and how the SAR gain is realized is dramatically different. This is a direct consequence of how the unique structure in each location is being amplified by SAR focusing and not an indication that mDD-SAR focusing performs better on one orbit compared to another.

Even though mDD-SAR focusing consistently succeeds in separating signal from noise, the degree of separation (i.e., the SNR) decreases for longer apertures. For orbit 10798 (see Fig. 8), the SNR decrease is marginal and the majority can be attributed to the small (1 to 1.5 dB) increase in the noise floor at longer (15 and 30 km) apertures. The SAR gain is relatively constant (pixel

power probabilities in the 60 to 70 dB range exhibit only minor variation). However, for orbit 10589 (see Fig. 7), in addition to the same small increase in the noise floor there are also significant reductions in SAR gain as the aperture is lengthened. For example, consider the portion of the orbit 10589 results near fast-time sample 550, where the SAR gain decreases from approximately 13 dB at 5 km [see Fig. 7(b)], to 8.5 dB at 15 km [see Fig. 7(c)], and to finally 6 dB at 30 km [see Fig. 7(d)]. An equivalent decrease in mean peak signal power with aperture length can also be observed in the general fast-time pixel power probability results [see Fig. 7(e)]. Similar to observations made during qualitative comparison, the decrease in SAR gain with increasing aperture length is due to the majority of orbit 10589 reflections being associated with flat and planar features as opposed to discrete point targets [9].

When applied across the entire radargram (as is done for Figs. 7 and 8), the pixel power probability metric yields a holistic view of mDD-SAR focusing and, as has been observed, the results are highly dependent on the nature of the target being imaged for that particular orbit (i.e., are there subsurface layers present, is the surface flat or dipping, etc.). However, a subtle yet important implication of this observation is that where there is strong variability in the nature of the target along an orbit,

local pixel power probability analyses may appear dramatically different compared to the holistic result.

It is not difficult to imagine such a scenario for orbit 10589 (see Fig. 3). If the same pixel power probability analysis were performed but considering only the portions of the radargrams between 65 and 90 s, quantitative patterns in SNR and SAR gain would likely be similar to those observed for the full radargram (i.e., SNR and SAR gain decrease with increasing aperture). In contrast, a pixel power probability analysis between 20 and 50 s would yield the opposite pattern of increasing SNR with aperture length. Because the nature of the radar reflectors imaged during orbit 10798 is more consistent (see Fig. 4), the pixel power probability metric is unlikely to present with the same spatial variability. Taken together, spatial variability in the pixel power probability results can be used to infer local scale changes in the radar scattering behavior of the target.

IV. SUITABILITY OF MODIFICATIONS FOR REASON DATA IDIOSYNCRASIES

Section II introduced the modifications made to the standard SHARAD delay Doppler algorithm in order to account for idiosyncrasies in REASON data and Section III demonstrated that the modified approach can be used to produce useful scientific results. However, the SHARAD data used for demonstration in Section III does not contain the same idiosyncrasies as future REASON data, and therefore, the appropriateness of the modifications has yet to be fully demonstrated. This section investigates the suitability of each modification using either existing or modified space-borne radar sounding datasets that mimic the behavior implicit in future REASON data.

A. Doppler Centroid Estimation

As MRO orbits Mars at approximately a 300 km altitude [17], the minimum distance between MRO and the mid-aperture nadir surface within a SHARAD synthetic aperture typically occurs at the mid-point of that aperture. This limits the ability to directly test the Doppler centroid estimation step in the mDD-SAR approach with SHARAD. Fortunately, the Mars Express spacecraft carries the MARSIS instrument and travels in a more elliptical orbit compared to MRO [14], [15]. MARSIS radar measurements are typically downlinked after significant on-board processing including range compression, ionospheric correction and Doppler filtering [15], which makes the majority of downlinked data ill-suited to the task of demonstrating the Doppler centroid estimation. However, limited lengths of unprocessed data have been downlinked and are available for download from the ESA. It is these data that are used to demonstrate the Doppler centroid estimation step in the mDD-SAR method.

The suitability of the Doppler centroid estimation procedure is demonstrated in Fig. 9 using an unprocessed section of MARSIS orbit 02665 acquired using the 4 MHz center frequency band. MARSIS orbit 02665 covers a topographically smooth portion of the Martian Southern Polar layered deposits and this lack of topography leads to an absence of diffraction hyperbola in the unfocused radargram. Fig. 9(a) presents the MARSIS

radargram after range compression and range line alignment. No ionospheric correction is performed as the data were acquired during the Martian night when ionospheric activity is minimal [29], [30].

The mDD-SAR $R(t)$ curve calculated for all range lines within the first synthetic aperture [dashed red lines in Fig. 9(a) and (d)] and is presented in Fig. 9(b). At this point in orbit 02665, Mars Express is shown to be consistently moving away from Mars as $R(t)$ increases across the aperture. The tangent to the $R(t)$ curve at the mid-aperture position is defined and its slope is used to estimate the expected Doppler centroid (3). Single-look data at the estimated Doppler centroid (-17.64 Hz) are then extracted after range and azimuth migration [see Fig. 9(c)] to complete delay Doppler SAR focusing for that synthetic aperture. It is clear from Fig. 9(c) that extracting focused data assuming a Doppler centroid of 0 Hz would not yield a correct result. The single-look focused 4 MHz radargram for this portion of MARSIS orbit 02665 is presented in Fig. 9(d) and is generated using a 30 km aperture, no range line interpolation and a unit SAR focusing interval (i.e., each range line is focused). As expected, there is a clear increase in signal strength after SAR focusing associated with the SAR gain.

As an alternative to the telemetry-based approach adopted in this article, the position of the Doppler centroid can also be derived from the radar sounding data themselves [31]. Data-derived Doppler centroids are used by the Italian SHARAD data processing team as an input into their chirp scaling SAR focusing algorithm [26], [27]. For Italian SHARAD data processing, the Doppler centroid is assumed to be the frequency that divides the Doppler energy spectra in two equivalent halves [32]. While this may be an appropriate assumption for SHARAD, which is in a near-circular orbit around Mars, the results observed in Fig. 9 suggest a more complicated situation when the radar acquires data along a more elliptical (e.g., MARSIS) or flyby (e.g., REASON) trajectory. Nonetheless, Fig. 10(a) presents a comparison of the telemetry-based estimates of the Doppler centroid used in this article (black points) to those reported in the Italian SHARAD RDR data products (the solid gray line) for SHARAD orbit 10589 [see Fig. 6(a)]. There is a very good agreement between the Doppler centroids derived from the spacecraft telemetry and those derived from the data as part of Italian SHARAD data processing. Along-track variability in the Italian data-derived Doppler centroids is a result of them being estimated only once in 20 s long data blocks while also attempting to account for variations in nadir Martian surface slopes [26], [27]. Similar results are also observed for SHARAD orbit 10798.

As discussed in [31], Doppler centroid estimation based on spacecraft telemetry will be subject to uncertainties in spacecraft position. Fig. 10(a) also presents the variability in the estimated Doppler centroids considering different uncertainty functions overlain onto the SHARAD 10589 spacecraft radius vector telemetry data. Uncertainties in spacecraft radius vector are assumed to vary linearly across the orbit (both upward and downward) and three different maximum uncertainty magnitudes are considered (50, 100, and 150 m). The modified spacecraft radius vector data are presented in Fig. 10(b) along

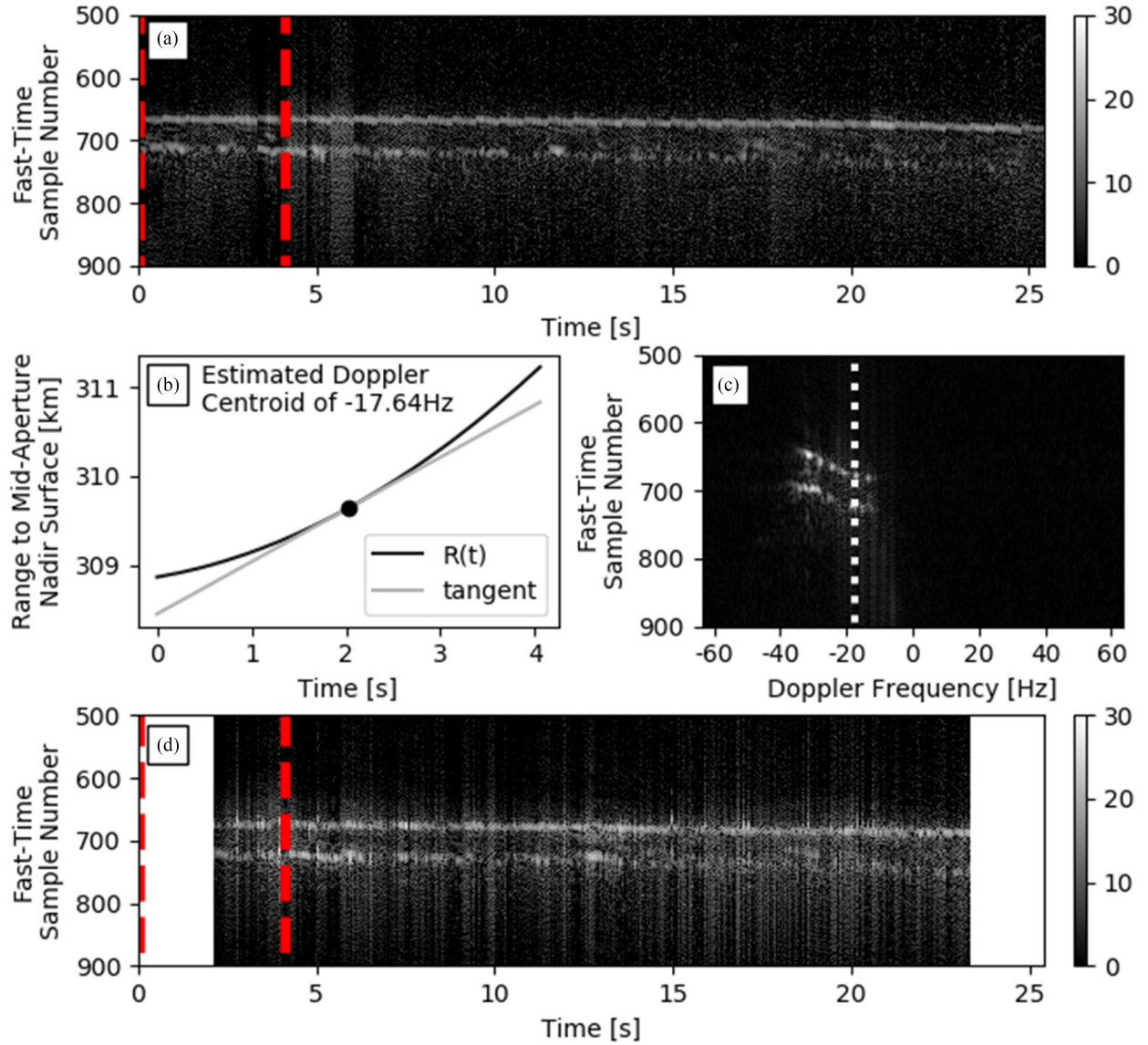


Fig. 9. Demonstration of Doppler centroid estimation step using an unprocessed MARSIS orbit 02665. (a) Range compressed and fast-time aligned radargram with the limits of the first synthetic aperture defined by vertical red lines. (b) Fitting a tangent to the $R(t)$ curve for the first aperture at the mid-aperture position to estimate the Doppler centroid. (c) Extraction of the focused data at the estimated Doppler centroid position. (d) The final single look modified delay Doppler focused radargram for all synthetic apertures. Results demonstrate the ability of the modified delay Doppler algorithm to handle radar sounding datasets acquired following an elliptical trajectory.

with the unmodified original. The addition of linearly varying uncertainties in spacecraft radial position introduces a bulk shift in the telemetry-estimated estimated Doppler centroids; with larger shifts being observed for larger uncertainty magnitudes. Note that even for the highest uncertainty magnitude (150 m), the telemetry-based estimate of the Doppler centroid does not significantly vary outside the range of data-derived Doppler centroids reported in the Italian SHARAD RDR data products.

Fig. 11 presents the portion of the mDD-SAR focused SHARAD 10589 radargram between 0 and 35 s as an RGB image where each channel presents a defined level of radial position uncertainty (R: -150 m to $+150$ m, G: unmodified, B: $+150$ m to -150 m). The focusing parameters used to generate the individual radargrams represented in Fig. 11 are the same as

those used to generate Fig. 3(d) and nongrayscale colors represent differences between the resulting SAR-focused radargrams. It is clear that the addition of radial positional uncertainty has minimal effect on the ability of the mDD-SAR focuser to recover overall topography and there are only minor highly localized variations in echo power at the edges of some reflectors. Even though smooth radial position uncertainties across an orbit do not appear to degrade the SHARAD focusing results, the effects over a Europa Clipper flyby that exhibits a greater change in spacecraft altitude warrants further consideration.

B. Range Line Interpolation

Even though MARSIS data can be used to demonstrate the suitability of the Doppler centroid estimation modification,

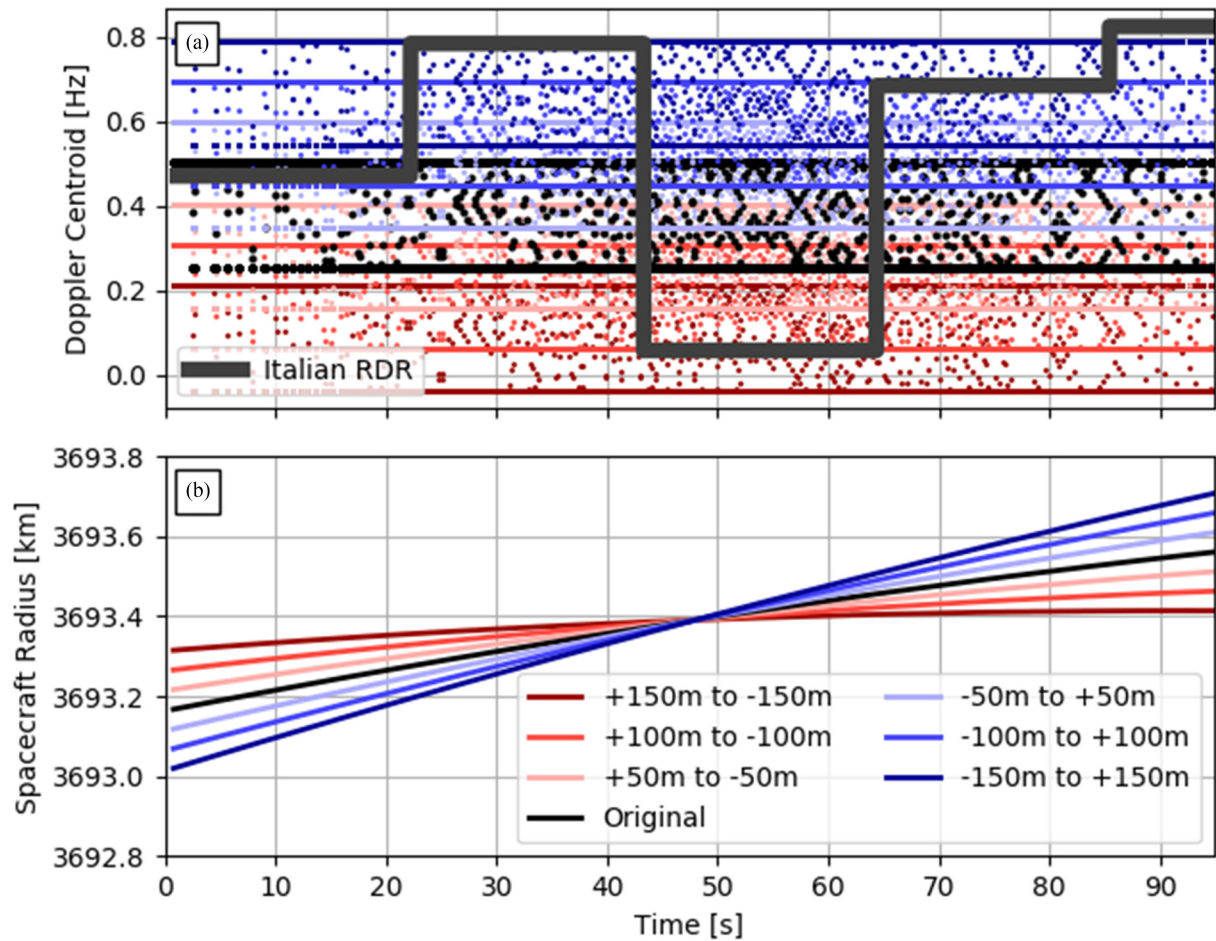


Fig. 10. Alongtrack variability in (a) telemetry-based (dots; some of which overlap and merge together into lines) and data-derived (gray line; as reported in Italian RDR) estimates of Doppler centroids and (b) spacecraft radius vector as a function of radial spacecraft positional uncertainty for SHARAD orbit 10589. Linearly-varying uncertainties in radial spacecraft position introduce bulk shifts in the telemetry-based estimates of the Doppler centroid, with larger shifts observed for larger uncertainty magnitudes. Even for the largest uncertainty magnitude (150 m), the telemetry-based estimates of the Doppler centroid do not significantly vary from the range of data-derived Doppler centroids.

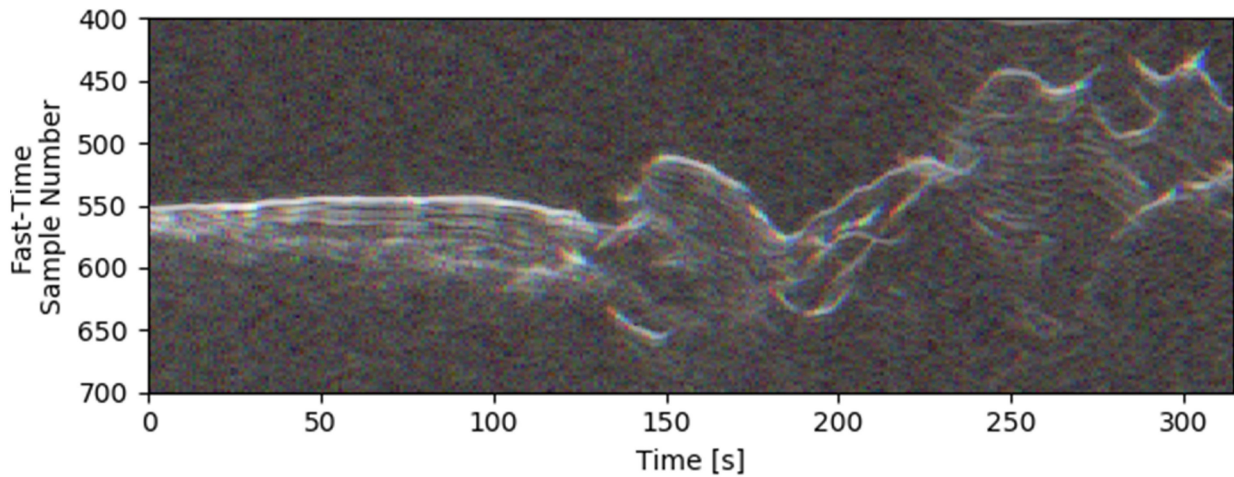


Fig. 11. RGB image of portion of the mDD-SAR focused SHARAD orbit 10589 radargram (0 to 35 s) where different channels consider different levels of linearly varying radial positional uncertainty (R: -150 m to $+150$ m, G: no modification, B: $+150$ m to -150 m). Deviations from grayscale then represent differences introduced by positional uncertainty. Overall surface topography is not affected by positional uncertainty with only minor variations in observed echo strengths.

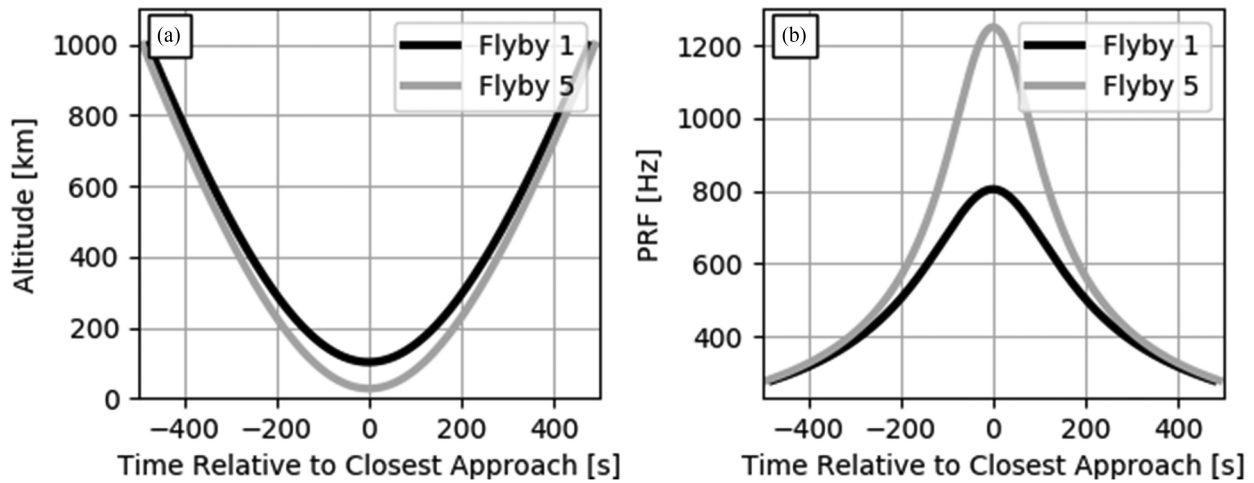


Fig. 12. Europa clipper (a) altitude and (b) instantaneous REASON PRF profiles for flybys 1 and 5 of the 17F12v2 trajectory.

neither MARSIS nor SHARAD directly mimics REASON's variable PRF. As such, unedited data from either instrument cannot be used to evaluate the suitability of the range line interpolation modification. The approach adopted for this article is therefore to construct facsimiles of REASON PRF profiles and interpolate SHARAD orbit 10589 telemetry and radar data onto sections of that PRF profile prior to SAR focusing. This alters the timing of SHARAD data collection such that it is more representative of REASON data acquisition. Robustness in this portion of the mDD-SAR approach is assessed by comparing the focused results after interpolation onto the REASON PRF facsimiles and the focused results when the constant SHARAD PRF is unaltered using the quality control framework introduced in Section III-B. Data from SHARAD orbit 10589 are used instead of those from MARSIS orbit 02665 because the dataset is longer (95 versus 25 s) and will cover a wider variation in PRF, and contains a greater topographic variability.

Facsimiles of REASON PRF profiles are constructed from SPICE data [33], [34] for two Europa flybys (flybys 1 and 5) in the Europa clipper mission 17F12v2 trajectory. Two flybys are considered as the distance of closest approach between Europa Clipper and Europa is not constant and therefore the required PRF profile differs for individual flybys. Fig. 12(a) presents the altitude profiles for Flybys 1 and 5. The closest approach distance varies from 100 km in flyby 1 to 25 km in flyby 5, but the maximum altitude considered for both cases is 1000 km. From the altitude profiles, the instantaneous PRF required to maintain the requisite Doppler bandwidth in order to discriminate an alongtrack surface target with a slant range equivalent to 3 km depth in Europa's ice shell is calculated [see Fig. 12(b)] [19]. There is a substantial (~ 400 Hz) difference in the PRF required for closest approach distances of 100 and 25 km.

Instantaneous PRF [see Fig. 12(b)] is constantly varying as it is a direct response to a constantly varying platform altitude [see Fig. 12(a)]. However, it is anticipated that a constantly changing PRF will be difficult to achieve in practice with REASON. In response, a concept similar to MARSIS frames is overlain onto the instantaneous REASON PRF profiles. In the context

of MARSIS, a frame is a length of time during which the data acquisition parameters (i.e., PRF, receive window opening times etc.) are fixed [15]. In this analysis, the instantaneous REASON PRF profiles [see Fig. 12(b)] are partitioned into 1200 frames, each roughly 0.8 s long with a fixed PRF. As high operational altitudes are involved, there will be situations where, in order to maintain PRF, signal transmission is required before echoes of the previous transmission are recorded. The transition to a new frame then cannot occur before all planned transmissions within the current frame are completed. In order to account for this in the facsimile REASON PRF profiles, for every frame except the first, the first two pulse repetition intervals (PRIs) of the new frame are dropped in order to allow all echoes from the previous frame to be recorded. This mode of operation will introduce time gaps in the datasets that appear as a reduced PRF between frames.

The results of partitioning the instantaneous REASON flyby 1 PRF profile according to the previously described procedures are presented as Fig. 13. This partitioned PRF profile represents the facsimile onto which SHARAD data will be interpolated. In Fig. 13(a), while the constant PRF within each partitioned frame is difficult to see, the substantial reductions in PRF associated with the PRI gaps between frames are clear. Successful partitioning of the instantaneous PRF profile to a constant PRF within each of the frames is shown in Fig. 13(b). An equivalent partitioned PRF profile is generated for flyby 5 but with different absolute PRF values due to the different flyby geometry.

After using the partitioned REASON PRF profiles for flybys 1 and 5 to define the timing associated with each simulated REASON range line, the SHARAD orbit 10589 unfocused radar and telemetry data are linearly interpolated onto that same timing profile. Four different interpolations (Trials) of the SHARAD orbit 10589 data onto 95 s long portions of the REASON PRF profile are performed for flyby 1 [see Fig. 14(a)] and three for flyby 5 PRF [see Fig. 14(b)]. Trial positions are selected such that they cover the critical portions of the flyby including where the PRF is maximal (around closest approach) as well as where the PRF is most quickly varying (approximately halfway between

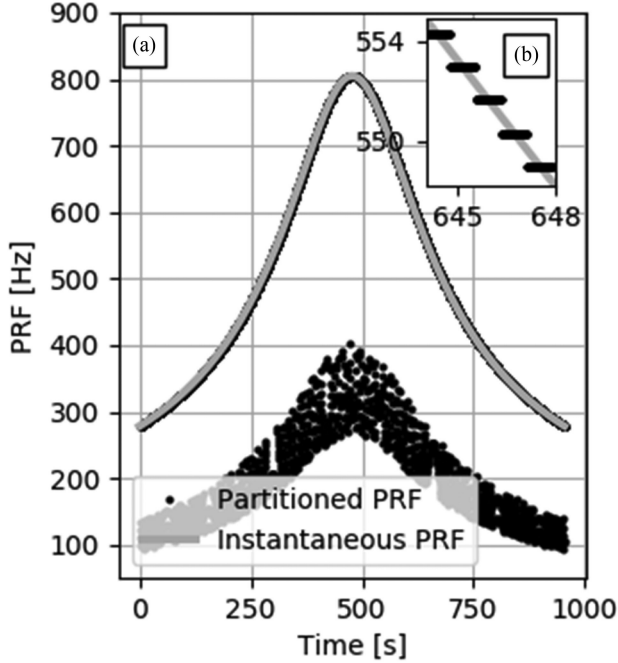


Fig. 13. Results of REASON flyby 1 PRF profile partitioning for (a) the complete flyby and (b) a zoomed-in section. Low PRFs at the bottom of the plot correspond to the gaps between frames.

1000 km and closest approach). These edited SHARAD data are then SAR focused using a 10 m ground track interpolation interval, a five sample SAR focusing interval, a 30 km aperture, and are multi-looked to a 400 m ground track range line interval (8 looks).

The stability of the mDD-SAR focusing approach with respect to variable REASON PRF profiles is evaluated using the pixel power probability quality control metric. Fig. 15 presents the mean pixel power probability results [again relative to the range compressed and ionosphere corrected radargram; Fig. 3(a)] for each Trial [flyby 1 in Fig. 15(a) and flyby 5 in Fig. 15(b)] as well unaltered SHARAD data focused with the same processing parameters. There is effectively no difference in how power in the focused radargrams is being reorganized even though the PRF profile of each Trial is different. Some very small variations are noticeable in the immediate vicinity of the noise floor (~ 57 dB), but in areas of higher power that correspond to the reflections of interest (> 65 dB; Fig. 3) the various Trials all agree with the unaltered result. It is therefore possible to conclude that the interpolation to a constant ground track interval modification made to the SHARAD delay Doppler SAR algorithm in order to account for both a variable PRF as well as the presence of data gaps is both successful and robust.

V. REVISITING THE ASSUMPTION OF DEPTH-INDEPENDENT SAR FOCUSING

Implicit in the decision to design a REASON SAR focusing algorithm based on the SHARAD delay Doppler approach [6] is the assumption that SAR focusing will be independent of depth. This is in contrast to the matched filter approach taken in LRS SAR focusing [9], which attempts to account for radar

wave refraction at interfaces between materials with different radar propagation velocities. In order to account for the effects of ray path refraction, LRS SAR focusing assumes that the trajectory of the spacecraft is perpendicular to the target surface. While this simplification is appropriate for when the platform altitudes are small (e.g., airborne radar sounding studies of Earth's glaciers and ice sheets [2], [7], [8]), it will rapidly breakdown as the platform altitude increases and the spherical nature of the target body need be accounted for (i.e., alongtrack distances can no longer be considered equivalent to ground track distances). For REASON, the situation is further complicated for Europa clipper's flyby trajectory [see Figs. 1(b) and 12(a)] and the fact that the only location where Europa Clipper will be travelling tangential to Europa is at closest approach. As such implementing a depth-dependent SAR focusing as presented in [9] is ill-suited for REASON. The modification of the matched filter approach for REASON geometries will be the subject of future investigations.

That being said, it is still worthwhile to consider the simplified geometry presented in [9] and assess the implications of assuming that predicted point target responses $[R(t)]$ used in REASON SAR focusing are depth-independent for an aperture centered on closest approach. Fig. 16(a)–(c) present the difference in predicted end-of-aperture Doppler phase shifts for depth-independent (mDD-SAR) and depth-dependent [9] point target responses at three depths in Europa's ice shell (one, two and three kilometers; ϵ_r of 3.15) as the aperture length (between 2 and 30 km) and the REASON altitude (between 25 and 500 km) are varied. VHF Doppler phase shifts are used for illustration as they will be greater than those for the HF (3). Fig. 16(d)–(f) presents the timing differences (expressed in the number REASON fast-time samples using a 12 MHz sampling frequency) between the ends of the depth-independent and depth-dependent responses for point targets at depth in Europa's ice shell. Finally, Fig. 16(g)–(i) present the associated SAR gain differences (mDD-SAR relative to matched filter) assuming every sampled point on the depth-dependent matched filter response exhibits a unit amplitude. The SAR gain estimates are determined by summing along the delay Doppler and matched filter responses. Where the two predicted point target responses overlap, delay Doppler and matched filter SAR gains both increase; however, where the responses deviate, no additional delay Doppler SAR gain is realized.

Based solely on the predicted point target responses, equivalence between the depth-independent (mDD-SAR) and depth-dependent [9] approaches is achieved when the two responses are indistinguishable. As such, Fig. 16(d)–(i) demonstrates that outside of using large apertures near closest approach, the proposed mDD-SAR approach is expected to be successful and REASON SAR focusing can be considered depth-independent. Even for Europa Clipper's most aggressive 25 km closest approach [flyby 5 in Fig. 12(a)], a six kilometer aperture can be used before any depth-dependent differences affect the SAR focusing of scatterers in the upper three kilometers of the ice shell. For a 100 km closest approach [flyby 1 in Fig. 12(a)], this maximum aperture length increases to more than 20 km.

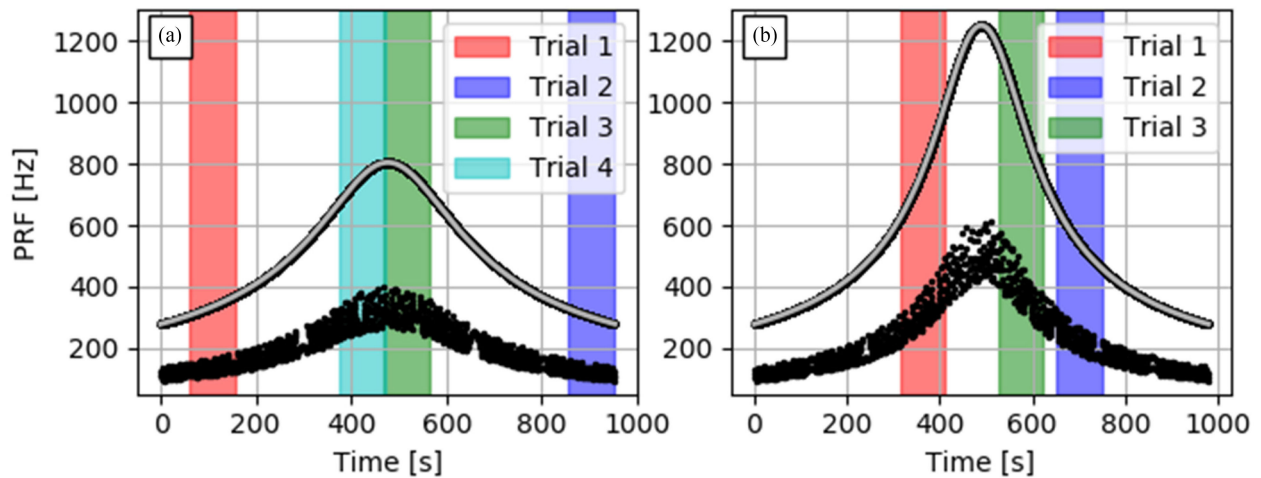


Fig. 14. Sections of the flyby (a) one and (b) five REASON facsimile PRF profiles onto which data from SHARAD orbit 10589 are interpolated. The various Trials cover the key portions of the PRF profile including the maximal PRF as well as where PRF is most rapidly varying.

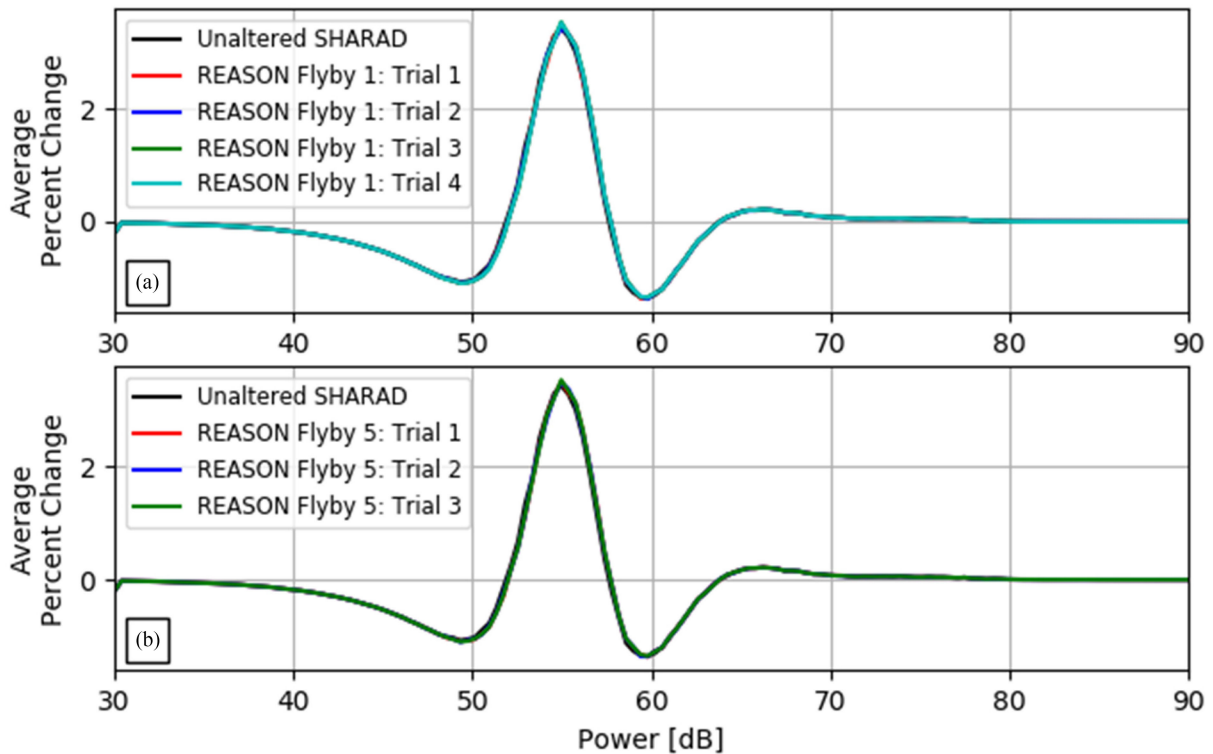


Fig. 15. Average percent change in the likelihood of an mDD-SAR-focused SHARAD 10589 radargram pixel exhibiting a specific power relative to the range compressed and ionosphere corrected radargram [see Fig. 3(a)] after interpolation onto REASON PRF profiles.

Implementing mDD-SAR focusing with large apertures centered on closest approach does increase the likelihood of introducing processing artefacts and misplaced reflectors in the output radargram. Ultimately though, this is dependent on energy being reflected from subsurface targets at the highest Doppler frequencies. If no high Doppler reflections from subsurface targets are generated (i.e., the subsurface is dominated by planar reflectors), there will be no reflected energy to be misplaced by a depth-independent predicted point scattering response. Under such conditions, using progressively longer aperture in SAR

focusing will result in an SNR decrease similar to what has been observed in Figs. 3 and 4. Features that may generate high Doppler frequency reflections within the upper three kilometers of the ice shell are likely to be related to corner reflectors, such as those at the edge of eutectics [35] or the bottom of cracks [36], [37]. However, artefacts introduced through the focusing of these features with large apertures, if they happen to be imaged near closest approach, can be used as an additional line of evidence that they are indeed point targets in the subsurface and not surface clutter.

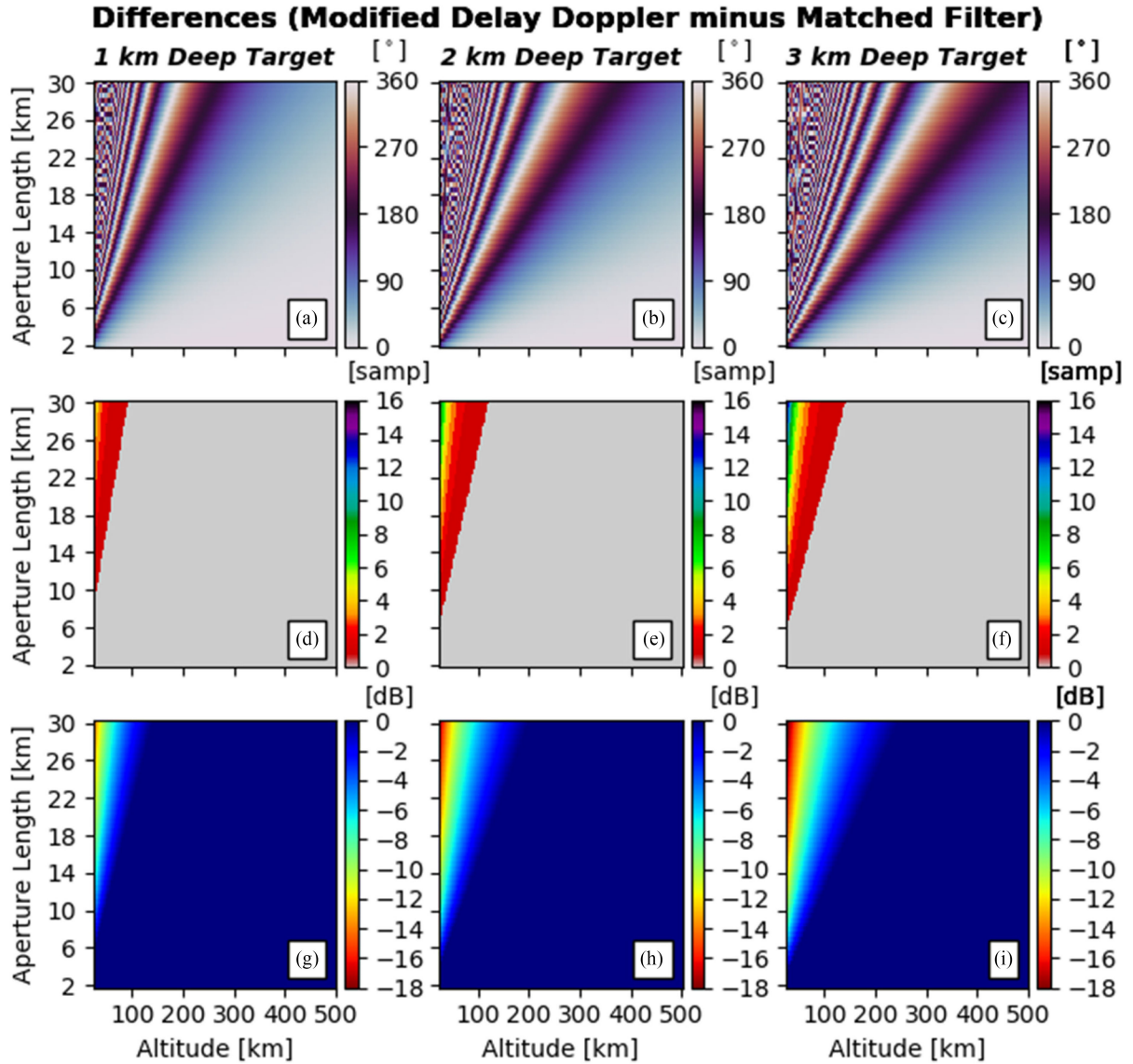


Fig. 16. Differences (modified delay Doppler minus matched filter) in predicted VHF Doppler phase shift [(a)–(c), in degrees], associated number of fast-time samples [(d)–(f) at the end of point target response functions], and SAR gain [(g)–(i), in dB] as the aperture length, platform altitude, and target depth [one (a), (d), and (g), two (b), (e), and (h), and three (c), (f), and (i) kilometers] are varied. The VHF fast-time sampling frequency is defined as 12 MHz. The assumptions of depth-independent SAR focusing is valid when there is no difference in the predicted shape of the subsurface point target response (d), (e), and (f) or SAR gain (g), (h), and (i) between the two methodologies.

VI. CONCLUSION

A flyby trajectory and desire to maintain a requisite Doppler bandwidth introduces key characteristics that differentiate future Europa Clipper REASON data from those produced by existing space-borne radar sounders. These in turn require a tailored SAR focusing methodology. Here we developed and demonstrated a mDD-SAR focusing approach that accounts for these idiosyncrasies by way of range line interpolation to a constant ground track interval and Doppler centroid estimation based on the predicted mid-aperture surface point target response. The mDD-SAR focusing approach, while designed to address REASON data idiosyncrasies, may also be applicable for use RIME data acquired during JUICE Europa flybys.

The ability of the mDD-SAR approach to successfully focus space-borne radar sounding data has been illustrated using data from two SHARAD orbits; 10598 and 10798. A quality control framework based on pixel power probabilities has also been introduced in order to evaluate SAR focusing performed with different processing parameters. This quality control framework readily communicates the relevant quantitative effects of SAR focusing such as SAR gain, noise floor reductions and SNR improvements. Furthermore, as the pixel power probability metric is highly sensitive to the nature of the target's radar reflectors, it can also be leveraged to assess local changes in radar scattering behavior. Finally, the implicit assumption of depth-independent SAR focusing has been compared with a depth-dependent approach for the extremely simplified case of a spacecraft travelling parallel to a flat surface. Depth independent

SAR focusing has shown to be viable assumption except when using long apertures at low altitudes. Overall, these results demonstrate the mDD-SAR approach to be a viable and robust option that is well-suited for the focusing of future REASON data.

REFERENCES

- [1] P. A. Rosen *et al.*, "Synthetic aperture radar interferometry," *Proc. IEEE*, vol. 88, no. 3, pp. 333–382, Mar. 2000.
- [2] J. J. Legarsky, S. P. Gogineni, and T. L. Akins, "Focused synthetic aperture radar processing of ice-sounder data collected over the Greenland ice sheet," *IEEE Trans. Geosci. Remote Sens.*, vol. 39, no. 10, pp. 2109–2117, Oct. 2001.
- [3] I. G. Cumming and F. H. Wong, *Digital Processing of Synthetic Aperture Radar Data: Algorithms and Implementation*. Boston, MA, USA: Artech House, 2005.
- [4] M. E. Peters, D. D. Blankenship, and D. L. Morse, "Analysis techniques for coherent airborne radar sounding: Application to west antarctic ice streams," *J. Geophys. Res. Solid Earth*, vol. 110, no. 6, pp. 1–17, Jun. 2005.
- [5] N. E. Putzig *et al.*, "Three-dimensional radar imaging of structures and craters in the martian polar caps," *Icarus*, vol. 308, pp. 138–147, Jul. 2018.
- [6] B. A. Campbell, N. E. Putzig, L. M. Carter, G. A. Morgan, R. J. Phillips, and J. J. Plaut, "Roughness and near-surface density of mars from SHARAD radar echoes," *J. Geophys. Res. E Planets*, vol. 118, no. 3, pp. 436–450, Mar. 2013.
- [7] M. E. Peters, D. D. Blankenship, S. P. Carter, S. D. Kempf, D. A. Young, and J. W. Holt, "Along-track focusing of airborne radar sounding data from west antarctica for improving basal reflection analysis and layer detection," *IEEE Trans. Geosci. Remote Sens.*, vol. 45, no. 9, pp. 2725–2736, Sep. 2007, [10.1109/TGRS.2007.897416](https://doi.org/10.1109/TGRS.2007.897416).
- [8] F. Hélière, C. C. Lin, H. Corr, and D. Vaughan, "Radio echo sounding of pine island glacier, west Antarctica: Aperture synthesis processing and analysis of feasibility from space," *IEEE Trans. Geosci. Remote Sens.*, vol. 45, no. 8, pp. 2573–2582, Aug. 2007, [10.1109/TGRS.2007.897433](https://doi.org/10.1109/TGRS.2007.897433).
- [9] T. Kobayashi *et al.*, "Synthetic aperture radar processing of kayuga lunar radar sounder data for lunar subsurface imaging," *IEEE Trans. Geosci. Remote Sens.*, vol. 50, no. 6, pp. 2161–2174, Jun. 2012, [10.1109/TGRS.2011.2171349](https://doi.org/10.1109/TGRS.2011.2171349).
- [10] D. D. Blankenship *et al.*, "REASON for Europa," in *Proc. 42nd COSPAR Sci. Assem.*, Jul. 2018, Art. no. B5.3-55-18.
- [11] D. D. Blankenship, D. A. Young, W. B. Moore, and J. C. Moore, "Radar sounding of Europa's subsurface properties and processes: The view from Earth," pp. 631–654, 2009.
- [12] L. Bruzzzone *et al.*, "RIME: Radar for icy moon exploration" in *Proc. Int. Geosci. Remote Sens. Symp.*, Jul. 2013, pp. 3907–3910.
- [13] T. Ono, and H. Oya, "Lunar radar sounder (LRS) experiment on-board the SELENE spacecraft," *Earth, Planets Space*, vol. 52, no. 9, pp. 629–637, Sep. 2000.
- [14] G. Picardi *et al.*, "Radar soundings of the subsurface of Mars," *Science*, vol. 310, no. 5756, pp. 1925–1929, Dec. 2005.
- [15] R. Jordan *et al.*, "The Mars express MARSIS sounder instrument," *Planet. Space Sci.*, vol. 57, no. 14/15, pp. 1975–1986, Dec. 2009, [Online]. Available: [10.1016/j.pss.2009.09.016](https://doi.org/10.1016/j.pss.2009.09.016)
- [16] R. Seu *et al.*, "SHARAD sounding radar on the Mars reconnaissance orbiter," *J. Geophys. Res. E Planets*, vol. 112, no. 5, pp. 1–18, May 2007.
- [17] R. Croci, R. Seu, E. Flamini, and E. Russo, "The shallow RADar (SHARAD) onboard the NASA MRO mission," *Proc. IEEE*, vol. 99, no. 5, pp. 794–807, May 2011, [10.1109/JPROC.2010.2104130](https://doi.org/10.1109/JPROC.2010.2104130).
- [18] B. Buffington, "Trajectory design concept for the proposed europa clipper mission," in *Proc. AIAA/AAS Astrodyn. Specialist Conf.*, Aug. 2014, pp. 1–17.
- [19] M. S. Haynes, E. Chapin, A. Moussessian, and S. N. Madsen, "Surface clutter discrimination analysis for radar sounding interferometry," *IEEE Trans. Aerosp. Electron. Syst.*, vol. 55, no. 2, pp. 989–1003, Apr. 2019, [10.1109/TAES.2018.2867689](https://doi.org/10.1109/TAES.2018.2867689).
- [20] M. S. Haynes, E. Chapin, J. Martin, and D. M. Schroeder, "Geometric power fall-off in radar sounding," *IEEE Trans. Geosci. Remote Sens.*, vol. 56, no. 11, pp. 6571–6585, Jun. 2018, [10.1109/TGRS.2018.2840511](https://doi.org/10.1109/TGRS.2018.2840511).
- [21] D. Castelletti *et al.*, "An interferometric approach to cross-track clutter detection in two-channel VHF radar sounders," *IEEE Trans. Geosci. Remote Sens.*, vol. 55, no. 11, pp. 6128–6140, Nov. 2017, [10.1109/TGRS.2017.2721433](https://doi.org/10.1109/TGRS.2017.2721433).
- [22] C. Gerekos *et al.*, "Martian roughness analogues of European terrains for radar sounder investigations" *Icarus*, vol. 358, 2020, Art. 11419.
- [23] G. Steinbrügge *et al.*, "The surface roughness of Europa derived from Galileo stereo images," *Icarus*, vol. 343, Jun. 2020, Art. no. 114197, [Online]. Available: [10.1016/j.icarus.2020.113669](https://doi.org/10.1016/j.icarus.2020.113669)
- [24] B. A. Campbell, N. E. Putzig, L. M. Carter, and R. J. Phillips, "Autofocus correction of phase distortion effects on SHARAD echoes," *IEEE Geosci. Remote Sens. Lett.*, vol. 8, no. 5, pp. 939–942, Sep. 2011, [10.1109/LGRS.2011.2143692](https://doi.org/10.1109/LGRS.2011.2143692).
- [25] B. A. Campbell, N. E. Putzig, F. J. Foss II, and R. J. Phillips, "SHARAD signal attenuation and delay offsets due to the martian ionosphere," *IEEE Geosci. Remote Sens. Lett.*, vol. 11, no. 3, pp. 632–635, Mar. 2013, [10.1109/LGRS.2013.2273396](https://doi.org/10.1109/LGRS.2013.2273396).
- [26] G. Alberti, D. Dinardo, S. Mattei, C. Papa, and M. R. Santovito, "SHARAD radar signal processing technique," in *Proc. 4th Int. Workshop Adv. Ground Penetrating Radar*, Jun. 2007, pp. 1–4.
- [27] R. Seu *et al.*, "SHARAD, a shallow radar sounder to investigate the red planet," in *Proc. IEEE Radar Conf.*, May 2008, pp. 1–4.
- [28] K. M. Scanlan, D. A. Young, G. Steinbrügge, C. Grima, S. D. Kempf, and D. D. Blankenship, "Quantitative approaches to assess the quality in synthetic aperture radar focusing of orbital radar sounding datasets," in *Proc. 51st Lunar Planet. Sci. Conf.*, Mar. 2020, pp. 1–2.
- [29] B. A. Campbell, and T. R. Watters, "Phase compensation of MARSIS subsurface sounding data and estimation of ionospheric properties: New insights from SHARAD results," *J. Geophys. Res. Planets*, vol. 121, no. 2, pp. 180–193, Jan. 2016, [10.1002/2015JE004917](https://doi.org/10.1002/2015JE004917).
- [30] A. Safaenili *et al.*, "Estimation of the total electron content of the martian ionosphere using radar sounder surface echoes," *Geophys. Res. Lett.*, vol. 34, no. 23, pp. 1–6, Dec. 2007.
- [31] S. N. Madsen, "Estimating the doppler centroid of SAR data," *IEEE Transaction Aerosp. Electron. Syst.*, vol. 25, no. 2, pp. 134–140, Mar. 1989, [10.1109/7.18675](https://doi.org/10.1109/7.18675).
- [32] S. Slavney, and R. Orosei, "Mars reconnaissance orbiter shallow radar reduced data record software interface specification," NASA Planetary Data Systems, 2007. [Online]. Available: https://pds-geosciences.wustl.edu/mro/mro-m-sharad-4-rdr-v1/mrosh_1001/document/rdrsis.pdf
- [33] C. H. Acton, "Ancillary data services of NASA's navigation and ancillary information facility," *Planet. Space Sci.*, vol. 44, no. 1, pp. 65–70, Jan. 1996.
- [34] C. Acton, N. Bachman, B. Semenov, and E. Wright, "A look towards the future in the handling of space science mission geometry," *Planet. Space Sci.*, vol. 150, Feb. 2017, pp. 9–12, Jan. 2018.
- [35] B. E. Schmidt, D. D. Blankenship, G. W. Patterson, and P. M. Schenk, "Active formation of 'chaos terrain' over shallow subsurface water on Europa," *Nature*, vol. 479, pp. 502–505, Nov. 2011.
- [36] R. J. Michaelides, and D. Schroeder, "Doppler-based discrimination of radar sounder target scattering properties: A case study of subsurface water geometry in Europa's ice shell," *Icarus*, vol. 326, pp. 29–36, Jul. 2019.
- [37] G. Steinbrügge *et al.*, "Brine migration and impact-induced cryovolcanism on Europa," *Geophys. Res. Lett.*, vol. 47, no. 21, Nov. 2020, Art. no. e2020GL090797.



Kirk M. Scanlan received the B.S. degree in geophysics from Western University, London, ON, Canada in 2011 and the M.A.E.S. degree in applied geophysics from TU Delft, Delft, The Netherlands, the M.S. degree in applied geophysics from ETH Zurich, Zurich, Switzerland, and the M.S. degree in applied geophysics from RWTH Aachen University, Aachen, Germany, in 2013, and the Ph.D. degree in geotechnical engineering from the University of Alberta, Edmonton, AB, Canada in 2018.

He is currently a Postdoctoral Fellow with the University of Texas Institute for Geophysics, University of Texas at Austin, Austin TX, USA. He is an Affiliate of the Europa Clipper Science Team associated with the Radar for Europa Assessment and Sounding: Ocean to Near-surface instrument. His research interests include radar signal processing, radar sounding of planetary bodies and cryospheres, and the intersection of near-surface geophysics and geotechnical engineering.



Duncan A. Young received the B.Sc (Hons.) degree in geological sciences from the University of Canterbury, Christchurch, New Zealand, in 1998, and a Ph.D. degree in geology from Southern Methodist University, Dallas, TX, USA, in 2003.

He is currently a Research Scientist with the University of Texas Institute for Geophysics, University of Texas at Austin, Austin TX, USA, within the Polar and Planetary Group. He has participated in 13 polar aerogeophysical expeditions, and is involved in Scientific Committee in Antarctic Research data coordination efforts. He is a Co-investigator on the Europa Clipper mission and the Lead for the Radar for Europa Assessment and Sounding: Ocean to Near-surface Investigation's Science Data System.

Dr. Young is a Member of the American Geophysical Union and the International Glaciological Society.



Cyril Grima received the A.D. degree in mechanical engineering from Poitiers University, Poitiers, France, in 2001, the B.S. degree in physics from Versailles and Grenoble University, Grenoble, France, in 2005, the M.S. degree in space technology from Toulouse University, Toulouse, France, in 2006, the M.S. degree in solid earth geophysics, and the Ph.D. degree in planetary science from Grenoble University, Grenoble, France, in 2007 and 2011, respectively.

He is currently a Research Associate with the Institute for Geophysics, University of Texas at Austin, Austin, TX, USA. He is a Co-Investigator for the Radar for Europa Assessment and Sounding: Ocean to Near-surface, a Collaborator for the Radar for Icy Moon Exploration Science Team, European Space Agency. He did two field seasons in Antarctica and two in Greenland to operate the airborne High Capability Radar Sounder through the ICECAP program. His research interests include the earth and planetary cryospheres through radar sounder observations.

Dr. Grima is a member of the American Geophysical Union.



Gregor Steinbrügge received the M.S. degree in physics from Freie Universität Berlin, Berlin, Germany, in 2013 and the Ph.D. degree from the Institute for Geodesy and Geoinformation Science, TU Berlin, Berlin, Germany, in 2018.

He is currently a Postdoctoral Fellow with the Department of Geophysics, Stanford University, CA, USA. He is an Affiliate of the Europa Clipper Science Team associated with the Radar for Europa Assessment and Sounding: Ocean to Near-surface instrument, the BepiColombo Laser Altimeter on Bepi-

Colombo, and the Ganymede Laser Altimeter on JUICE. His current research is on tidal interactions of bodies in our solar system, ice geophysics, as well as radar and laser geodesy.



Donald D. Blankenship received the B.S. degree in geology from Eastern Illinois University, Charleston, IL, USA, in 1978, and the M.S. and Ph.D. degrees in geophysics from the University of Wisconsin, Madison, WI, USA, in 1982 and 1989, respectively.

He is currently a Senior Research Scientist with the Institute for Geophysics, Jackson School of Geosciences, University of Texas at Austin, Austin, TX, USA. He has been the funded PI or Co-PI on over 30 data acquisition and analysis projects. He has more than 25 years of experience leading airborne

and ground-based field campaigns in Antarctica and was the Chief Scientist and PI for all U.S. National Antarctic Aerogeophysics, from 1994 to 2002. He is also the PI on the Radar for Europa Assessment and Sounding: Ocean to Near-surface on NASA's Europa Clipper mission. His research interests include understanding earth's ice sheets and the underlying lithosphere through coupled geophysical observations, as well as planetary studies involving radar sounding investigations.

Dr. Blankenship is a member of the American Geophysical Union.



Scott D. Kempf received the B.S. and M.S. degrees in computer sciences from the University of Wisconsin, Madison, WI, USA, in 1990 and 1992, respectively.

He is currently a Senior Software Engineer with the University of Texas Institute for Geophysics, Jackson School of Geosciences, University of Texas at Austin, Austin TX, USA. He has participated in seven polar aerogeophysical expeditions. He maintains and processes data from Antarctica, the Arctic, and Mars, a dataset exceeding 200 TB.